



TALLINN UNIVERSITY OF TECHNOLOGY

SCHOOL OF ENGINEERING

Department of Materials and Environmental Technology

Sb₂S₃ Thin Film Solar Cell For Semi-transparent Applications

Õhukesekilelised Sb₂S₃ Poolläbipaistvad Päikesepatareid

MASTER THESIS

Student: Mohammad Kadkhodaei

Student code: 214602KAYM

Supervisors:

Sajeesh Vadakkedath Gopi

Nimish Juneja

Tallinn 2023

AUTHOR'S DECLARATION

Hereby I declare, that I have written this thesis independently.

No academic degree has been applied for based on this material. All works, major viewpoints, and data of the other authors used in this thesis have been referenced.

"....." May 2023

Author: Mohammad Kadkhodaei

/signature/

Thesis is in accordance with terms and requirements

"....." May 2023

Supervisor: Sajeesh Vadakkedath Gopi

/signature/

Accepted for defense

"....." May 2023

Chairman of theses defense commission:

/name and signature/

Non-exclusive license for reproduction and publication of a graduation thesis¹

I, Mohammad Kadkhodaei,

1. grant Tallinn University of Technology free license (non-exclusive license) for my thesis "Sb₂S₃ Thin Film Solar Cell For Semi-transparent Applications", supervised by Ph.D. students Sajeesh Vadakkedath Gopi and Nimish Juneja ,

1.1 to be reproduced for the purposes of preservation and electronic publication of the graduation thesis, incl. to be entered in the digital collection of the library of Tallinn University of Technology until the expiry of the term of copyright;

1.2 to be published via the web of Tallinn University of Technology, incl. to be entered in the digital collection of the library of Tallinn University of Technology until the expiry of the term of copyright.

2. I am aware that the author also retains the rights specified in clause 1 of the non-exclusive license.

3. I confirm that granting the non-exclusive license does not infringe other persons' intellectual property rights, the rights arising from the Personal Data Protection Act, or rights arising from other legislation.

24.05.2023

¹ The non-exclusive licence is not valid during the validity of access restriction indicated in the student's application for restriction on access to the graduation thesis that has been signed by the school's dean, except in case of the university's right to reproduce the thesis for preservation purposes only. If a graduation thesis is based on the joint creative activity of two or more persons and the co-author(s) has/have not granted, by the set deadline, the student defending his/her graduation thesis consent to reproduce and publish the graduation thesis in compliance with clauses 1.1 and 1.2 of the non-exclusive licence, the non-exclusive license shall not be valid for the period.

Faculty of Chemical and Materials Technology

THESIS TASK

Student: Mohammad Kadkhodaei, 214602KAYM
Study program, KAYM Materials and Processes for Sustainable Energetics
main specialty: materials for sustainable energetics
Supervisor(s): Ph.D. student, Sajeesh Vadakkedath Gopi, +372 54420493
Ph.D. student, Nimish Juneja, +37253622820

Thesis topic:

(in English) Sb_2S_3 Thin Film Solar Cell For Semi-transparent Applications
(in Estonian) Õhukesekilelised Sb_2S_3 Poolläbipaistvad Päikesepatareid

Thesis main objectives:

1. To gain an understanding of the fundamentals of thin film solar cells and conduct literature research on Sb_2S_3 based solar cells employing different hole transport materials.
2. To successfully fabricate Sb_2S_3 solar cells by using ultrasonic spray pyrolysis to deposit electron transport layer - TiO_2 and absorber - Sb_2S_3 . Deposit P3HT and Spiro-OMeTAD as Hole Transport Materials (HTM) using spin coating.
3. Conduct morphological, optical, and electrical characterization of the fabricated solar cells using SEM, XRD, UV-VIS, J-V, and EQE measurements.
4. To study the impact of the HTM layer thickness on the solar cell performance, by employing a systematic approach in which the thickness is optimized by changing the concentration of the HTM precursor solution.
5. To compare the performance of the solar cells targeting semitransparency with HTMs - P3HT and optimized Spiro-OMeTAD.

No	Task description	Deadline
1.	USP and spin coating deposition of the first set (Glass/FTO/P3HT or Spiro-OMeTAD) and the second set (Glass/FTO/TiO ₂ /Sb ₂ S ₃ /P3HT or Spiro-OMeTAD) of samples.	
2.	USP and spin coating deposition of the third set of samples (glass/FTO/TiO ₂ /Sb ₂ S ₃ /P3HT or Spiro-OMeTAD/Au), followed by solar cell characterization.	
3	Solar cell performance analysis (J-V, EQE) for samples from third set.	
4.	Analysis of acquired data and thesis preparation	

Language: English

Deadline for submission of thesis: 24th May 2023.

Student: Mohammad Kadkhodaei May 2023

/signature/

Supervisor: Sajeesh Vadakkedath Gopi May 2023

/signature/

Co-supervisor: Nimish Juneja May 2023

/signature/

Head of the study program: Professor Sergei Bereznev May 2023

/signature/

Contents

PREFACE	8
List of abbreviations	10
INTRODUCTION	12
1. THEORETICAL BACKGROUND	14
1.1 Solar cells	14
1.1.1 Basics of solar cells	14
1.1.2 Principle of solar cells	14
1.1.3 Thin-film solar cell structure	15
1.2 Types of solar cells	17
1.2.1 Amorphous Silicon Solar Cell	17
1.2.2 Cadmium Telluride Solar Cell	17
1.2.3 Copper Indium Gallium Selenide Solar Cells	18
1.2.4 Monocrystalline Silicon Solar Cell	18
1.2.5 Polycrystalline Silicon Solar Cell	18
1.3 Sb_2S_3 Absorber	19
1.4 Hole Transport Layer	22
1.4.1 P3HT	22
1.4.2 Spiro-OMeTAD	23
1.5 Deposition Methods	24
1.5.1 Spin-Coating	25
1.5.2 Spray pyrolysis	26
1.5.3 Thermal Evaporation	27
1.5.4 Sputtering	28
1.6 Material Characterization Methods	30
1.6.1 X-Ray Diffraction	30
1.6.2 Scanning Electron Microscopy	31
1.6.3 UV-VIS Spectroscopy	32
1.7 Solar Cell Characterization Methods	33
1.7.1 Current Density-Voltage measurement (J-V)	33
1.7.2 External quantum efficiency (EQE)	34
1.8 Summary of theoretical background and aims of the Thesis	36
2. EXPERIMENTAL	38
2.1 Fabrication of solar Cell	38
2.1.1 Cleaning and Preparation of substrate (Glass/FTO)	38
2.1.2 Deposition of the Electron Transport Layer (TiO_2) by ultrasonic spray pyrolysis	39
2.1.3 Deposition of the absorber (Sb_2S_3) by ultrasonic spray pyrolysis	40
2.1.4 Spiro-OMeTAD precursor preparation and deposition by spin coating	41
2.1.5 P3HT precursor preparation and deposition by spin coating	41

2.1.6 Deposition of metal contacts by thermal evaporation	42
2.2 Material characterization	42
2.3 Solar cell characterization	42
3. RESULTS AND DISCUSSION	44
3.1 Structural properties of Sb_2S_3 films	44
3.2 Application of HTMs in solar cells	46
3.2.1 Electrical Characterization	46
3.2.2 Optical Characterization	51
CONCLUSION	54
SUMMARY	56
REFERENCES	57

PREFACE

The following thesis was conceived by Professor ILONA OJA ACIK and executed in the Laboratory for Thin Film Energy Materials located at Tallinn University of Technology. My deepest gratitude goes to my supervisors, Ph.D. students Sajeesh Vadakkedath Gopi and Nimish Juneja, for their careful consideration of all aspects of my thesis and for their extraordinary ability to devote sufficient time to me even during periods of intense workload. Professor Sergei Bereznev, who undertook me under his wing and selected me for this program, which was one of my finest accomplishments in life, deserves many thanks.

This study was funded by the Estonian Research Council project PRG627 "Antimony chalcogenide thin films for next-generation semi-transparent solar cells applicable in electricity producing windows", the Estonian Research Council project PSG689 "Bismuth Chalcogenide Thin-Film Disruptive Green Solar Technology for Next Generation Photovoltaics", the Estonian Centre of Excellence project TK141 (TAR16016EK) "Advanced materials and high-technology devices for energy recuperation system", and the EU H2020 program under the ERA Chair project 5GSOLAR grant agreement No 952509.

Short summary

The thesis focuses on the impact of hole transport materials (HTM) on the performance of Sb_2S_3 -based solar cells for semi-transparent applications. Poly(3-hexylthiophene) (P3HT) and Spiro-oMeTAD are the two hole-transporting materials (HTMs) that have been investigated for use in Sb_2S_3 -based solar cells. Solar cells were fabricated in the glass/FTO/ TiO_2 / Sb_2S_3 /HTM/Au configuration where TiO_2 and Sb_2S_3 layers were deposited using ultrasonic spray pyrolysis. The HTMs were spin-coated and the Au contacts were thermally evaporated. The impact of the HTM solution's concentration on the performance of Sb_2S_3 solar cells was studied. Three concentrations of Spiro-OMeTAD precursor solutions were prepared in Chlorobenzene solvent; 60 mM solution referred to as Spiro1x, 30 mM referred to as Spiro2x, and 15 mM referred to as Spiro4x in this study. The morphological, optical, and electrical properties of the fabricated solar cell devices were studied using SEM, UV-vis spectroscopy, current-voltage (JV), and External Quantum Efficiency (EQE) measurements. Fabricated devices with optimized Spiro- oMeTAD as HTM yielded a power conversion efficiency of 3.1% while the cells with P3HT yielded 3.9%. As compared to P3HT devices, the transparency of the solar cell stack with Spiro-oMeTAD was enhanced by

over 20%. The study demonstrates the successful fabrication of semi-transparent Sb_2S_3 solar cells with two of the conventionally used HTMs.

Keywords: Thin film solar cells, Sb_2S_3 solar cells, hole transport material, P3HT, Spiro-OMeTAD

List of abbreviations

ALD	Atomic layer deposition
AVT	Average Visible Transmittance
α -Si	Amorphous silicon
as-dep	As-deposited (sample)
BSE	Backscattered electrons
CBD	Chemical bath deposition
CdTe	Cadmium telluride
CIGS	Cadmium indium gallium selenide
c-Si	Crystalline silicon
CSP	Chemical spray pyrolysis
CVD	Chemical vapor deposition
DSSC	Dye-sensitized solar cell
E_C	Conduction band minimum
E_F	Fermi level energy
E_g	Band gap energy
E_V	Valence band maximum
EQE	External quantum efficiency
ETL	Electron transport layer
FF	Fill factor
FTO	Fluorine-doped tin oxide
HTM	Hole transport material
ICDD	International Centre for Diffraction Data
ITO	Indium tin oxide
I_{sc}	Short circuit current

JCPDS	Joint Committee on Powder Diffraction Standards
Mono-Si	Monocrystalline Silicon Solar Cell
P3HT	Poly(3-hexylthiophene)
PCE	Photoconversion efficiency
PCDTBT	Poly [N-9'-heptadecanyl-2,7-carbazole-alt-5,5-(4',7'-di-2-thienyl-2',1',3'-benzothiadiazole)]
PEDOT:PSS	Poly(3,4-ethylenedioxythiophene)-poly(styrenesulfonate)
PV	Photovoltaics
PVD	Physical vapor deposition
Sb ₂ S ₃	Antimony trisulfide
SEM	Scanning electron microscopy
TiO ₂	Titanium dioxide
USP	Ultrasonic spray pyrolysis
UV-Vis	Ultraviolet-visible spectrophotometry
V _{oc}	Open circuit voltage
VTD	Vapor transport deposition
XRD	X-ray diffraction

INTRODUCTION

The globe has relied on fossil fuels to supply energy and address this problem during the past century, but there is a limited amount of these resources. The energy crisis remains and intensifies despite extensive attempts to address it. The stockpiles may not be replenished for many hundreds of thousands of years. Interestingly, even if humanity possessed an inexhaustible source of this sort of fuel, it'd still be forced to cope with the present problem.

In our modern world, 87% of greenhouse gas emissions worldwide can be attributed to the generation of energy, which relies mostly on fossil fuels. This phenomenon has led to global warming. The average global surface temperature is a statistic that may be used to indicate the effect of greenhouse gasses on Earth. The global land and ocean temperature anomalies chart illustrates information about the deviation from a specific period's global average surface temperature in Celsius degrees. The chart considers the average global surface temperature between the years 1991 to 2000 as the basis and shows the deviation from that basis between 1880 and 2021. The graph indicates that from 1880 to 1940, the difference from the base temperature was consistently negative. Meaning that during this period the global surface temperature was roughly 0.25 on average, cooler than the years 1991 to 2000. Beginning in 1940, there was a shift in direction, and the deviation became positive for the first time. Since 1978, the deviation has risen fast to new heights, with brief intervals of decline [1].

Human society can no longer just depend on fossil fuels to meet the world's ever-increasing energy needs. Because of this, finding long-term solutions for energy needs is a top priority for humanity. The unique qualities of solar energy, such as an infinite supply and global availability, make it present among the most promising renewable energy sources. Solar energy is the most plentiful renewable energy source. According to several papers and measurements, the sun emits at a rate of $3.8 \times 10^{23} kW$ out of which approximately $1.8 \times 10^{14} kW$ is intercepted by our planet Earth [2].

The majority of solar radiation reaches the planet as heat and energy. The bulk of the energy is lost when moving through the atmosphere owing to cloud absorption, reflection, and scattering events. However, research indicates that the quantity of solar radiation that reaches the earth's surface after passing through the atmosphere is more than sufficient to meet the global energy demands [3].

Solar energy is attractive for many reasons other than only its inexhaustibility and abundance. Solar energy has nearly no negative effect on the ecology and environment, primarily because it does not emit carbon dioxide and is independent of

fossil fuels [4]. In addition, solar energy may be employed in developing and undeveloped nations, as well as in villages and remote areas of developing nations, owing to its affordability and ease of application and access [5].

Scientists now rely on Photovoltaic Technology (PV) to capture and convert solar energy into power. The distribution and intensity of solar radiation are two major factors that have a significant impact on the efficiency of PV technologies, and these factors vary greatly from country to country because they depend on a country's location on the earth's surface and the average amount of solar radiation it receives annually. According to the *global horizontal irradiation map*, Asian nations have the largest capacity to receive solar radiation. This suggests that in such nations, solar energy may become the primary and, if the necessary infrastructure and technology for storage and transition are available, the only source of energy required [6].

Some disadvantages are limiting humanity from using solar energy as the primary or exclusive source of energy generation at the current time. Expensive energy storage, a dependence on the weather, a high initial cost or necessary capital, and the necessity for a vast landscape to generate adequate energy are among the primary disadvantages. Solar energy is still one of the most, if not the most, promising and environmentally friendly methods for meeting the world's energy needs in the future [7].

1. THEORETICAL BACKGROUND

1.1 Solar cells

A photovoltaic cell, commonly referred to as a solar cell, converts sunlight into electrical energy. In response to light absorption, the cell's semiconductor design allows the synthesis and separation of charges, resulting in the generation of electricity. Solar panels are made of solar cell modules connected in series or parallel configurations.

1.1.1 Basics of solar cells

In an isolated atom that is not subjected to a significant external force, the electrons have varying levels of energy. When atoms unite to form a crystal, two continuous energy bands are generated: the valence band and the conduction band. The band gap (E_g) refers to the region between these energy states. Band gap energy represents the minimum energy required to excite an electron from the valence band to the conduction band. Since the absorber layer operates on this principle, the band gap is a fundamental and significant factor in the development of solar cells. The absorber layer is a semiconducting material that is often thought of as the core of all thin-film solar cells. This layer absorbs the photons and excites electrons into the conduction band using the energy from photons to generate photocurrent. It is crucial to use an absorber layer with an appropriate band gap so that electrons can move to a higher energy level by absorbing the energy from photons. The band gap of semiconductors may range from 0.5 to 3 eV. Electrons in a semiconductor material with a narrow band gap might enter the conduction band at room temperature, leaving behind holes in the valence band. Due to this feature, some semiconductors are able to conduct electricity even at room temperature [8] [9]. Figure 1 illustrates the band gap structure in semiconductors.

1.1.2 Principle of solar cells

Photovoltaics (PV) Technology enables us to catch solar energy and convert it into electrical power. The photovoltaic effect is the core of PV technologies and the operating concepts upon which PV technologies are founded. In PV cells, the photovoltaic effect occurs. In their most basic form, solar cells consist of two distinct semiconductor materials. The photons of solar radiation are absorbed by the semiconductor material when the cell is exposed to sunlight.

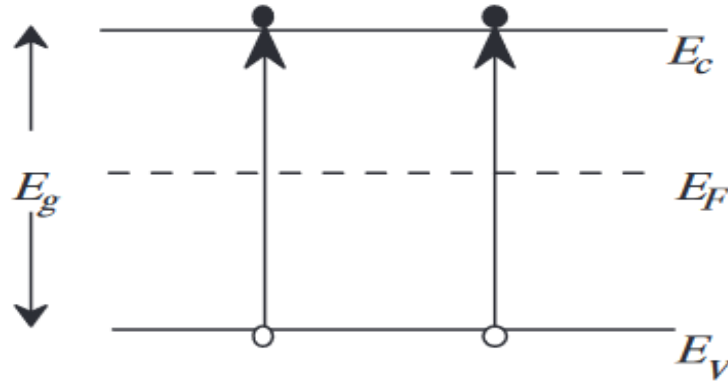


Figure 1. Semiconductors' energy band representations [8]

When light of an appropriate wavelength strikes a semiconductor, energy from the photon is transferred to the electrons in the semiconductor's atoms. Therefore, the electrons vacate their original place inside the atom, leaving behind “holes”. The first semiconductor layer, identified as n-type, is negatively charged and contains an abundance of electrons. The other layer is known as p-type and is positively charged due to its abundance of holes. When these two layers are connected, a p/n junction is formed at the interface, which generates an electrical field. To further grasp this concept, we may imagine the p/n junction layer at the interface as an insulator that prevents electrons from passing through. This is because, at the contact, extra electrons flow from the n-type semiconductor to the p-type, resulting in the formation of a p/n junction, a thin layer at the interface. Due to this electric field, the electrons in the n-type semiconductor flow toward the negative surface, while the holes in the p-type material travel toward the positive surface. By externally linking the PV cell's terminals, electrons move toward the holes, resulting in the flow of current via the circuit [10]. Figure 2 summarizes the information into 5 essential stages needed to generate current in a solar cell.

1.1.3 Thin-film solar cell structure

Obviously, solar cells consist of more than just absorbent layers. Numerous components must come together to form a functional solar cell. A conventional thin-film solar cell is composed of a front contact, window layer, absorber layer, and lastly a rear contact. Since the light must reach the absorber layer for the solar cell to function, the two layers above it, the window layer and front contact, must be transparent to a substantial amount of solar radiation. The front contact is often a thin layer of conductive oxide

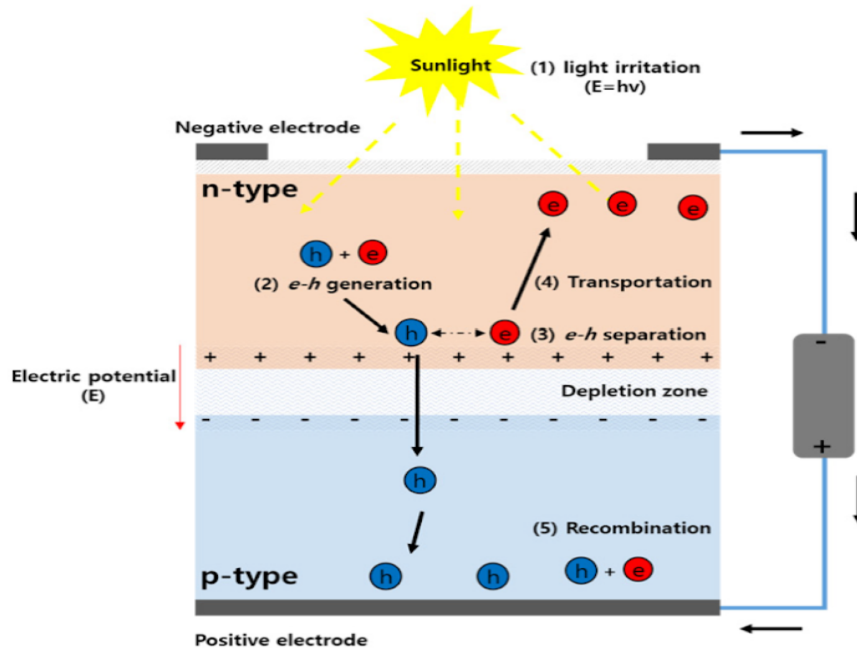


Figure 2. The working principle of solar cells with a p-n junction structure [11].

coated on a glass substrate; common examples are fluorine-doped tin oxide (FTO) and indium-doped tin oxide (ITO). The goal of conductive oxide is to capture electrons and route them via the external circuit in order to generate electricity. Transparency and low sheet resistance are two of the features that enable the conductive oxide layer to do its duty with great effectiveness [12]. What separates the front contact layer from the absorber is the window layer. Typically, this layer is an n-type semiconductor with a wide bandgap. Since the window layer is in close interaction with the absorber, it serves a significant role in the formation of the p/n junction region, also referred to as the depletion region. Titanium dioxide, which was employed as the n-type semiconductor material in this experiment, Cadmium sulfide, and zinc oxide are some of the most often used window layer materials [13]. The absorber layer follows. Typically, the absorber layer is a p-type semiconductor. This layer is primarily responsible for charge separation, which, coupled with contact with the window layer, results in a p/n junction and forces electrons and holes toward opposing surfaces, where they will be collected by an external circuit. Cadmium telluride, antimony trisulfide, α -Si, and Copper indium gallium selenide (CIGS) are some of the most common absorbers used in the solar cell industry [12]. The back contact is often composed of a highly conductive metal such as gold (Au), silver (Ag), or copper (Cu) and serves mainly to aid in charge extraction and transfer to the external circuit [14].

1.2 Types of solar cells

Since the invention of the first practical solar cells less than 30 years ago, scientists and academics have been tirelessly developing new solar cells and optimizing existing ones to reach the maximum power conversion efficiencies. Consequently, there are several varieties of solar cells, but not all of them can compete in the race for supremacy. Owing to the availability of silicon, solar cells based on silicon now dominate the market due to their high efficiency and cheap manufacturing costs. Silicon is the second most plentiful known element after oxygen and comprises around 27.7 percent of the earth's crust. This section examines some of the most common and promising types of solar cells [15].

1.2.1 Amorphous Silicon Solar Cell

Amorphous or non-crystalline silicon, also known as a-Si, has existed in the marketplace for more than 15 years, making it the most developed thin film solar cell material. This form of silicon is advantageous in that it can be deposited at low temperatures (down to 75 degrees Celsius), allowing it to be coated on polymers. Additionally, the cheap production cost contributes to its capacity to compete with other kinds of solar cells. Nevertheless, amorphous silicon cannot be employed as a single-layer cell owing to its significant degradation when exposed to sunlight, which results in decreased light absorption and, thus, decreased efficiency. The maximum efficiency of this kind of silicon solar cell is between 7 and 10 percent. The usage of amorphous silicon solar cells is common in pocket calculators but rare in powering buildings [16].

1.2.2 Cadmium Telluride Solar Cell

Cadmium is a very dangerous and lethal substance. It is one of the top ten most lethal elements known. It seems to become less hazardous when combined with tellurium, but this does not make it safe. Cadmium Telluride photovoltaics took up over half of the thin film industry back in 2013 and accounted for 5.1% of global PV output despite the toxicity of this material. This may be due to the fact that Cadmium Telluride is the only thin film method capable of competing on a cost basis with the dominant crystalline silicon technology. Among various solar cell technologies, it offers the lowest carbon impact and the quickest payback period. CdTe can indeed be recycled at the end of its useful life, but public worries about its toxicity and the scarcity of tellurium are significant impediments to its commercial manufacture. The greatest theoretical efficiency recorded

of this kind of solar cell is between 28% and 30%, whereas the maximum efficiency observed in the lab by "First Solar" is 22.1% [15].

1.2.3 Copper Indium Gallium Selenide Solar Cells

Due to its greater absorption coefficient than other thin film absorber materials, CIGS requires a far thinner layer, making it a very intriguing material. As a consequence, it may be placed on a flexible substrate to create solar cells that are exceedingly flexible and lightweight. Since the standard deposition process for thin film technologies happens in a high-temperature setting, the optimal performance of CIGS solar panels is achieved by using a glass substrate. However, developments in the low-temperature deposition of CIGS cells permit the use of other substrates. On a laboratory scale, the efficiency of CIGS solar cells was claimed to exceed 20%, whereas commercial panels typically had an efficiency of 12-14% [17].

1.2.4 Monocrystalline Silicon Solar Cell

Mono-Si is one of the most essential technical materials since its usage as the basic material in almost all electronic devices used by human civilization has facilitated the information revolution. Silicon with a single crystalline structure may also include trace amounts of other elements to alter its characteristics. According to reports, this form of silicon solar panel has the best efficiency at 17-22%, requiring less room to generate the same amount of energy. They also operate well during low sunlight or foggy conditions, however, they are the most costly solar cells on the market, making them difficult for most people to acquire [18].

1.2.5 Polycrystalline Silicon Solar Cell

Polycrystalline solar panels became the first commercially accessible solar cells back in 1981. Unlike monocrystalline cells, polycrystalline panels are not cut during the production phase. In its place, polycrystalline silicon is produced by pouring molten silicon into a square-shaped mold. As a result, they are substantially more cost-effective, as marginal amounts of silicon are wasted during manufacture. Polycrystalline is inferior to its monocrystalline sister in terms of performance. Again, the lower material purity leads to an efficiency range of 13-16% for polysilicon PV settings. Therefore, polycrystalline is less space-efficient. In addition, polycrystalline materials have a lower heat endurance than monocrystalline materials, meaning they are less

effective at high temperatures [15]. Figure 3 shows the difference in the appearance of monocrystalline and polycrystalline silicon solar cells.

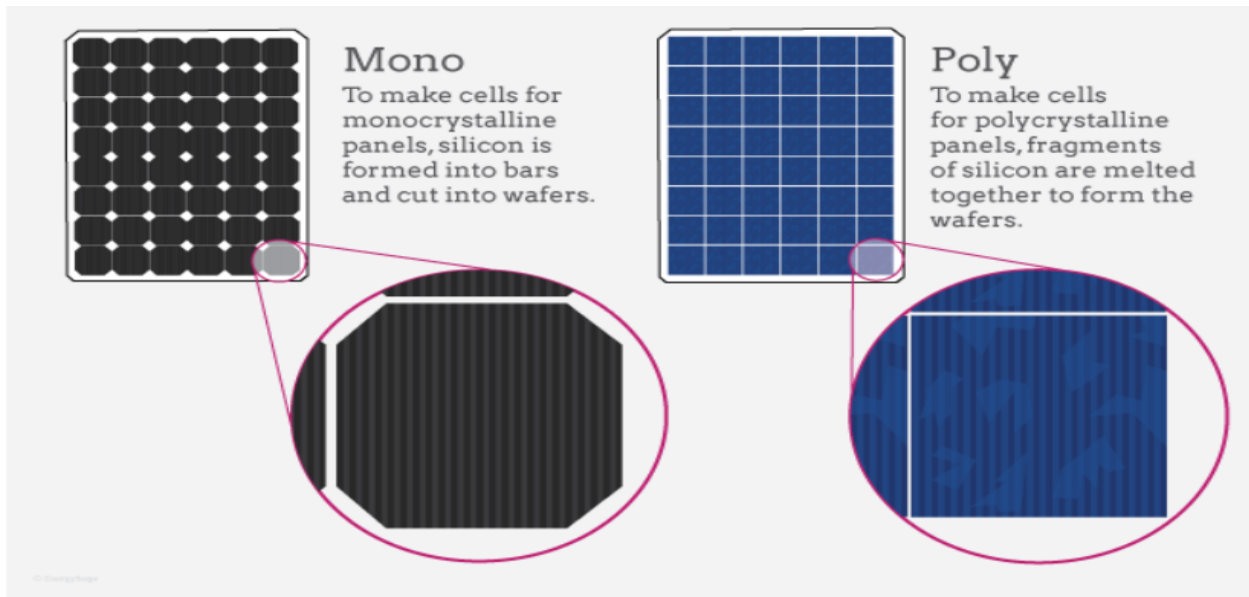


Figure 3. Monocrystalline vs polycrystalline Silicon solar panels [19]

1.3 Sb_2S_3 Absorber

Antimony trisulfide is a potential material that is primarily employed as the absorber layer in thin-film solar cells. There are a number of factors that make this material appealing and promising, including non-toxic and abundant structural elements, a high absorption factor, and a melting temperature of around 550 degrees Celsius, which allowed researchers and scientists to synthesize high-quality crystalline films at low temperatures typically below 350 degrees Celsius. Furthermore, antimony trisulfide seems to have a band gap between 1.7-1.8 eV, making it an excellent candidate for PV applications [20].

Sb_2S_3 is composed of an endless amount of $(\text{Sb}_4\text{S}_6)_n$ chains widely known among scientists as ribbons oriented in the direction [001]. A core unit of Sb_2S_3 crystal, one individual ribbon consists of a pair of Sb_2S_3 trigonal and a pair of SbS_5 square pyramids. As a result, ribbons are connected to produce zigzag layers perpendicular to the [100] surface. Bond lengths(d), between Sb and S atoms in Sb_2S_3 , could be roughly

separated into three groups: the [001] direction where the Bond length is less than 2.5 angstrom, [010] direction where the bond length falls between 2.58 and 3.25 angstroms, and finally [100] direction where bond length is roughly between 3.45 and 3.74 angstroms. Experiments have confirmed that covalent bonding is predominant inside the ribbon along the c-axis, while between ribbons and sheets, atoms are joined by weaker forces, notably along the [100] axis [14]. Figure 4 illustrates the crystal structure of antimony trisulfide.

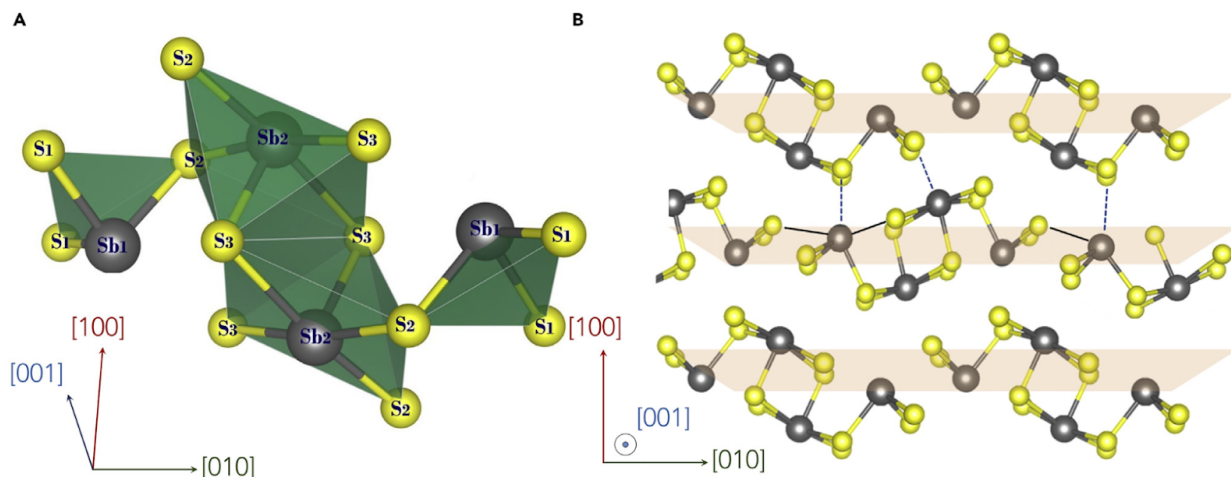


Figure 4. Crystal structure of Antimony trisulfide(Sb_2S_3) [14] [21] **(A)** Visualizing an individual ribbon consisting of a pair of Sb_2S_3 trigonal and a pair of SbS_5 square pyramids **(B)** Visualizing crystal structure of Sb_2S_3 on [001] sheet. Please note that sulfur atoms are shown as yellow and antimony atoms are visualized as gray.

Due to its advantageous properties, Sb_2S_3 has been utilized as the absorber layer for various types of solar cells. Sb_2S_3 has been paired by various research groups with a variety of ETL and HTM layers to increase the overall efficiency of the solar cell with the hope that it will one day be able to compete with silicon-based solar cells, the predominant industrial material at present. The conventional used HTMs, P3HT and Spiro-OMeTAD, have shown promise in improving device performance. The choice of HTM may depend on factors such as hole mobility, interfacial contact, and the specific device architecture [21]. Based on the literature review conducted for this thesis, Table 1 presents a comprehensive summary of Sb_2S_3 -based solar cells and the attained power conversion efficiency in more than a decade of experiments.

Table 1. Summary of literature review of Sb₂S₃-based solar cell prepared with different deposition methods and with different organic and inorganic HTMs.

HTM	Cell configuration	Sb ₂ S ₃ method of deposition	Sb ₂ S ₃ Thickness (nm)	Solar cell Parameters				Ref.
				V _{oc}	J _{sc}	FF	PCE	
No HTM	ITO/CdS/Sb ₂ S ₃ /Au	VTD	1800	710	15.7	43	4.7	[22]
P3HT	ITO/TiO ₂ /Sb ₂ S ₃ /P3HT/ Ag	ALD	155	732	9.3	62	4.3	[23]
P3HT	ITO/TiO ₂ /Sb ₂ S ₃ /P3HT/ Au	USP	150	618	6.0	51	1.9	[21]
P3HT	ITO/TiO ₂ /Sb ₂ S ₃ /P3HT/ Au	USP	100	693	13.8	58	5.5	[24]
Spiro-OMeTAD	FTO/TiO ₂ /ZnCl ₂ /Sb ₂ S ₃ / Spiro-OMeTAD/Au	Spin coating	162	650	17.7	62	7.1	[25]
Spiro-OMeTAD	FTO/CdS/Sb ₂ S ₃ / Spiro-OMeTAD/Au	CBD	214	757	17.4	60	8.0	[26]
V ₂ O ₅	FTO/TiO ₂ /Sb ₂ S ₃ /V ₂ O ₅ / Au	Spin coating	130	590	15.3	53	4.8	[27]
NiO _x	FTO/TiO ₂ /Sb ₂ S ₃ /NiO _x / Au	Spin coating	100	590	14.5	40	3.5	[28]
CuSCN	FTO/TiO ₂ /Sb ₂ S ₃ / CuSCN/Au	CBD	20	565	12.6	54	3.8	[29]
V1236	FTO/TiO ₂ /Sb ₂ S ₃ / HTM/Au	USP	90	612	13.8	46	3.9	[30]

1.4 Hole Transport Layer

1.4.1 P3HT

Poly(3-hexylthiophene), often referred to as P3HT, is a well-known low-bandgap polymer with a bandgap value of 1.8 eV [59]. P3HT is a widely used and well-understood polymer within organic photovoltaics studies. It is generally stable and due to the ease of synthesis and compatibility with high-throughput manufacturing processes, it is also scalable to some degree. P3HT is among a handful of polymers now accessible in amounts greater than 10 kilograms, making it among the few viable possibilities for commercial organic photovoltaics and wide-area usage. Moreover, in comparison to more amorphous polymers, its semi-crystalline structure of it, is unique in establishing an acceptable morphological length for bulk heterojunction organic photovoltaics from a variety of solvents and processing conditions, while also offering excellent charge transport capabilities [31]. Several studies have reported improved device performance with the incorporation of P3HT as an HTM in Sb_2S_3 solar cells. Figure 5 shows the chemical structure of P3HT.

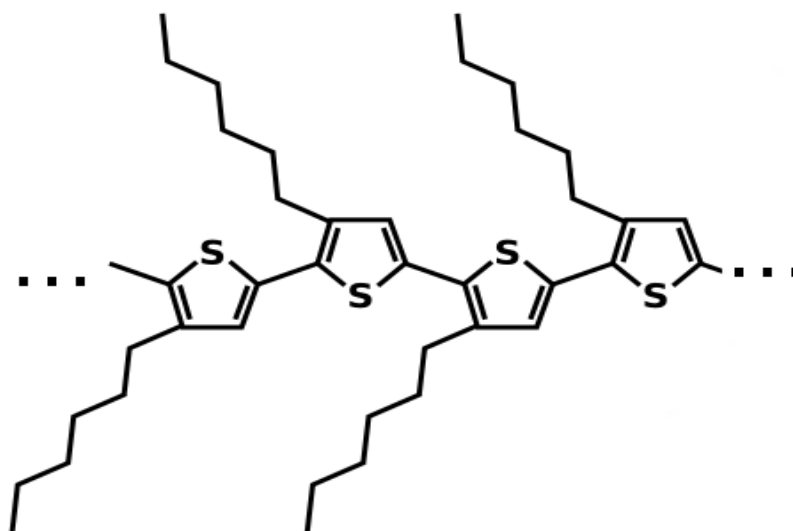


Figure 5. Chemical structure of Poly(3-hexylthiophene) [30]

1.4.2 Spiro-OMeTAD

In the 1990s, 2,2',7,7'-Tetrakis[N,N-di(4-methoxyphenyl)amino]-9,9'-spirobifluorene, often known as Spiro-OMeTAD, was originally synthesized as a stable amorphous material with good conductivity. It was initially used in perovskite solar cells (PSC) in 2012, exhibiting a remarkable 9.7% efficiency and a vastly increased stability over liquid junction PSCs. By oxidizing Spiro-OMeTAD to Spiro-OMeTAD⁺, it is possible to employ it to serve as the hole transparent layer in photovoltaic cells. Despite the fact that the electrical characteristics of doped Spiro-OMeTAD allow high-efficiency semiconductors in a laboratory setting, its stability poses a significant obstacle. While Spiro-OMeTAD has a melting temperature of 245 degrees Celsius, even pristine Spiro-OMeTAD is susceptible to crystallization at 100 degrees Celsius, which disrupts contact at its surfaces. Even with this drawback, Spiro-OMeTAD is still a popular material to be used as a hole transport layer in photovoltaic cells for specific applications while researchers try to achieve higher efficiency and better stability that enables this material to be used in a wider range of applications [32]. Figure 6 illustrates the structure of Spiro-OMeTAD.

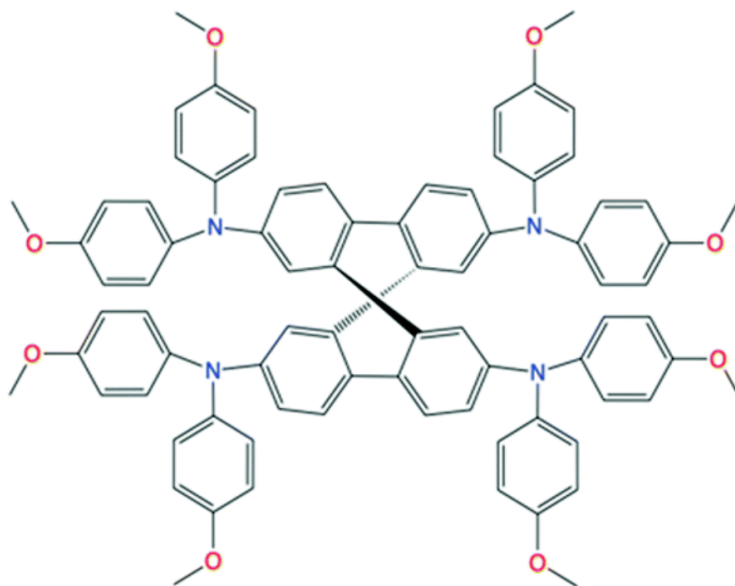


Figure 6. Chemical structure of Spiro-OMeTAD [33]

1.5 Deposition Methods

Thin-film deposition is the process of placing a thin layer of material on top of another material until all desired layers have been deposited and the solar cell is ready for testing. Each layer serves a distinct purpose, such as absorbing the sunlight, enhancing the device's hardness, altering its conductivity, or modifying its optical properties. The substrate is the base layer upon which other layers are deposited. Chemical deposition methods and physical deposition methods are the two broad categories of deposition techniques. Physical vapor deposition (PVD) techniques are used to vaporize a desired substance which then can be deposited on a substrate or another layer. No chemical reaction will occur during the PVD process. Chemical deposition, on the other hand, involves a reaction wherein the precursor self-assembles and coats the substrate. It is subdivided further into chemical vapor deposition and chemical bath deposition [34]. Figure 7 illustrates the categorization of deposition methods. In this research, this section discusses the principles of some of the more common methods.

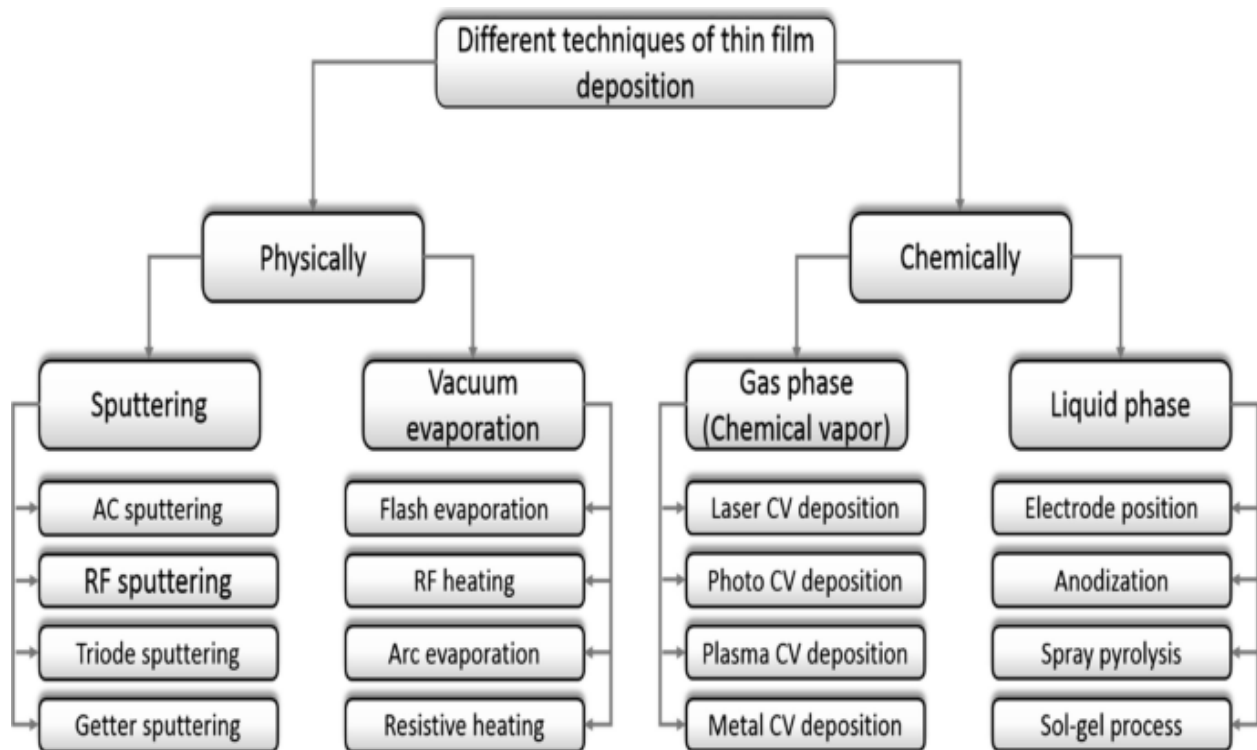


Figure 7. Thin film deposition techniques classification [35]

1.5.1 Spin-Coating

Spin-coating is a method utilized to deposit low-thickness films using high-speed rotational force which spreads out the precursor solution over the surface of the substrate in a uniform way. The precursor is applied on the substrate's surface, and rotation pushes the solution to distribute while the solvent quickly evaporates to generate a homogeneous coating layer [36]. In this work, this method was employed to deposit films of P3HT and Spiro-OMeTAD on a glass/FTO/TiO₂/Sb₂S₃.

There are two techniques to add the precursor: either while the substrate is spinning, which is referred to as a dynamic process, or before the spinning begins, which is referred to as a static process. In this study, a static process was utilized for the deposition of the films [36].

Evaporation temperature, spinning velocity, spinning duration, and precursor viscosity are the parameters that highly affect the final film thickness. Therefore, having control over factors such as coating solution volume, rotating speed, rotational duration, and solution concentration is crucial to get the desired films. To achieve crystallization of the films, the spin coating procedure is often followed by one or two annealing steps [37]. Thin films with thicknesses ranging from a few nanometers to a few micrometers can be prepared by spin coating. Typically, the substrate's rotational speed exceeds 10 spins per second or 600 rpm [38]. Figure 8 illustrates the four phases of the spin-coating procedure: deposition, spin-up, spin-off, and evaporation.

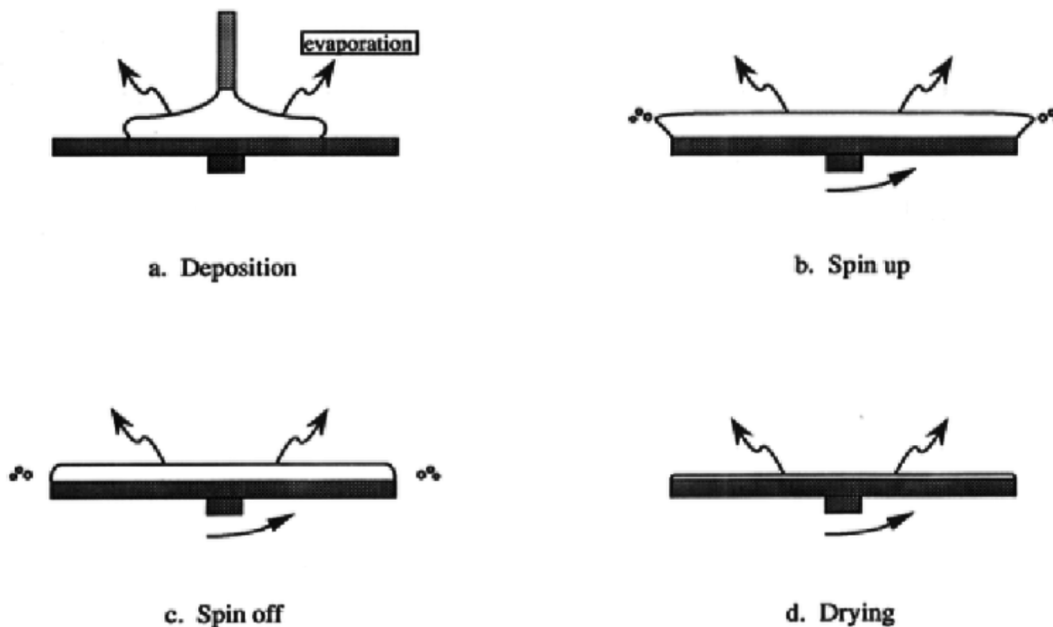


Figure 8. Four stages of spin coating deposition [39]

1.5.2 Spray pyrolysis

Similar to spin coating, spray pyrolysis is a solution-based chemical deposition technique. Spray pyrolysis permits the deposition of very thin and uniform coatings on a large surface area in an inexpensive way. Additionally, less precursor solution may be used for broad surface deposition. The precursor mixture of the target film is sprayed over a heated substrate in this procedure, resulting in the formation of a chemical compound. To prevent the formation of undesirable byproducts, the reactants are selected such that these byproducts are decomposed and removed at or before the deposition temperature. A precursor solution, a heat source for the substrate, a gas to carry the fume (often air or nitrogen), an atomizer, and a temperature controller are required to accomplish a spray pyrolysis deposition. The three most popular types of atomizers are air blast, ultrasonic, and electrostatic. The function of the atomizer is to create a vapor from the precursor solution that can be sprayed onto the heated substrate. Each of the above-described atomizers does the purpose in a unique manner. Ultrasonic atomizers perform the task by using ultrasonic frequencies to generate a short wavelength for fine atomization, whereas electrostatic atomizers expose the solution to an electric field to achieve atomization, and air blast atomizers expose the desired solution to a flow of air to generate a vapor of the desired solution [40].

Spray pyrolysis is an excellent method for metal oxide deposition owing to its simplicity of usage, low cost of equipment, and low maintenance needs. Compared to vacuum machinery, energy consumption is minimal. The quality and characteristics of the deposited layer are highly sensitive to the deposition process parameters. For example, the surface temperature of the substrate strongly affects the crystal structure, degree of crystallinity and other physical properties of the produced film [40]. Figure 9 illustrates the setup of a simple spray pyrolysis system.

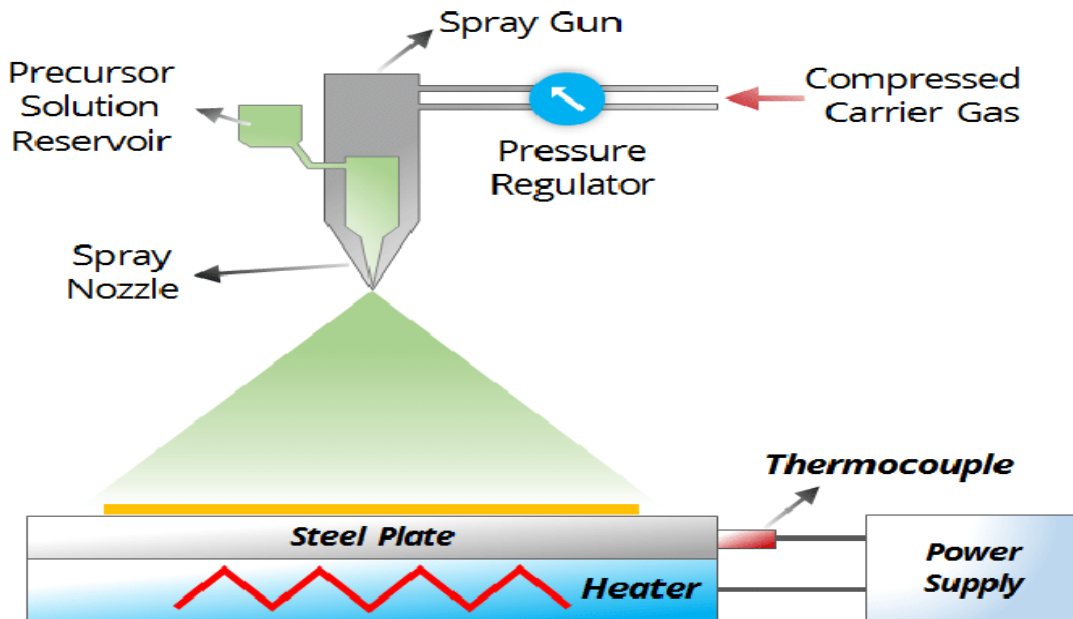


Figure 9. Operating setup of a simple Spray Pyrolysis system [41]

1.5.3 Thermal Evaporation

Thermal evaporation is one of the most common techniques of physical vapor deposition. Thermal Evaporation consists of heating material in a chamber with a high vacuum, usually less than 10^{-5} torr, to a point that generates vapor pressure. A relatively modest vapor pressure seems sufficient to generate a vapor cloud within a vacuum chamber. This evaporated substance is now a vapor flow that crosses the chamber, forming a thin film of the material on the substrate. In most cases, the desired depositing material is heated up to its melting temperature and is thus liquid. Consequently, it is often located close to the bottom of the container. The substrate, however, is being held in an inverted position in the chamber's upper fixtures in a way that the desired surface for coating is faced down and toward the heating source so that as the vapor starts to fill up all the space in the chamber, it also coats the surface of the substrate [42]. Figure 10 shows the operation principle of thermal evaporation deposition.

There are two fundamental methods for heating the raw material. A filament is a basic electrically resistive heat element that is used in a technique often known as filament evaporation. There are a variety of physical shapes of resistive evaporation filaments, such as "boats"; simply, thin sheet metal pieces of appropriate high-temperature

materials, tungsten for instance, which were created purposely for this task. The filament source provides the comfort of low voltage yet requires a very high current of several hundred amps [43].

Electron Beams, or E-Beams, are another popular heat source. E-Beam systems often have additional safety measures due to the "high tech" nature of this kind of material heating, which typically includes 10,000 volts of voltage level. The source is an E-Beam "gun" in which a short, extremely hot filament boils electrons off, which then get accelerated by the noticeably high voltage to generate a high-energy electron beam. The produced beam is magnetically guided toward the crucible containing the substance. This warms the metal, which is kept in a water-cooled pit to avoid its destruction. It is extremely typical for commercially marketed E-Beam guns to feature numerous crucibles, allowing them to simultaneously hold a variety of materials and shift between them to perform multilayer processing [44].

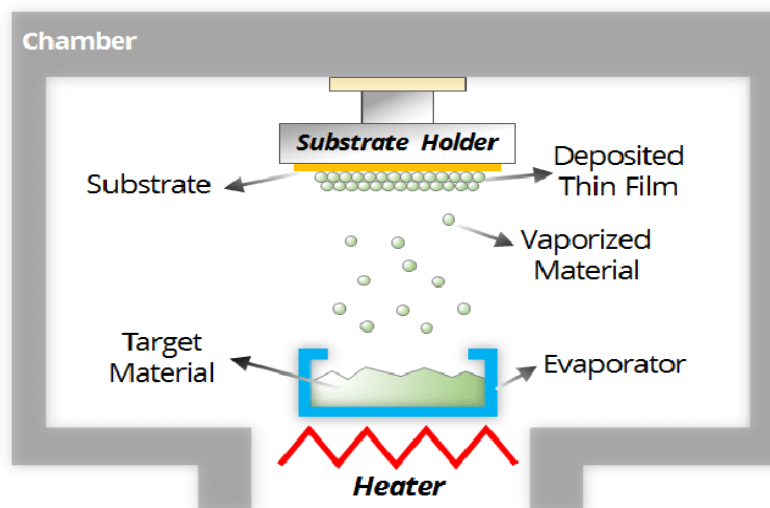


Figure 10. Operating principle of a simple Thermal Evaporation system [45]

1.5.4 Sputtering

Another frequent physical vapor deposition method is sputtering. The sputtering technique for the deposition of thin films requires inserting a regulated gas, often argon, into the vacuum chamber and electrically activating a cathode to create a plasma. "Target" represents the surface side of the cathode exposed to plasma, which is the desired material to be deposited onto the substrates. The gas atoms, in this process, lose electrons within the plasma to form positively charged ions, which ultimately are

accelerated toward the "target". If the kinetic energy is sufficient, the plasma will force the atoms of the target material out of their original position. This will result in the formation of a vapor stream from the sputtered material that crosses the chamber and sticks to the substrate [46]. Figure 11 illustrates the operating principles of the sputtering method.

Rare gases are used in the sputtering process because they will not react with the coating material which prevents the formation of unwanted byproducts. Argon is frequently the preferred rare gas in the sputtering process due to two primary causes; Firstly, Argon makes up approximately 1% of the atmosphere and, therefore, is fairly inexpensive; and secondly, Argon's mass which is approximately 39.95 amu is a decent match to a wide variety of metals in the periodic table regarding proper collisional momentum transfer [47].

A clean substrate surface is essential to achieve effective deposition. Before inserting substrates in the vacuum chamber, they must undergo the necessary cleaning and handling procedures [46].

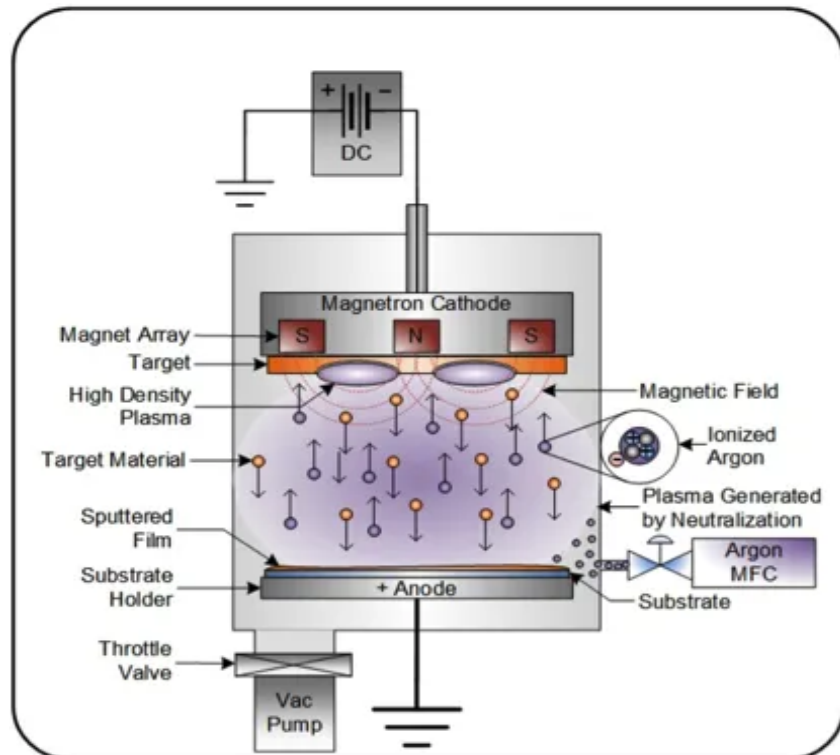


Figure 11. Operating principle of sputtering deposition technique [47]

1.6 Material Characterization Methods

1.6.1 X-Ray Diffraction

X-Ray diffraction, often known as XRD, is a method used to examine the properties of crystalline materials. Structure, crystal orientation and degree of crystallinity, grain size, and defects are just a few of the details that XRD may reveal about the desired material. This procedure begins with the emission of X-Rays, which are then directed to the sample. X-rays are electromagnetic radiation waves that are measured on a nanoscale. As a consequence of collisions with the material's structure, X-rays scatter and produce interferences. Owing to both constructive and destructive interferences, this produces a pattern of low and high intensities. Due to the fact that each material has unique distances between its atomic planes (D-spacings), the sample's structure may be determined by collecting diffracted X-rays and matching the peaks arising from D-spacings to established standards [48].

$$n\lambda = 2d \sin \theta \quad (1)$$

The operating premise of XRD is based on Bragg's law (Figure 12). Bragg's rule states that diffraction will occur if the interaction between the x-rays and the material satisfies the following conditions: the incidence angle must be equal to the scattering angle, and the path length difference must be equal to an integer number of wavelengths. This permits a state of peak intensity, which subsequently permits the computation of the crystal structure's specifics [48].

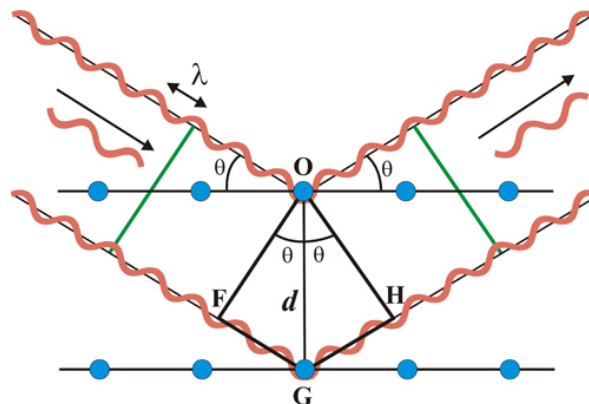


Figure 12. The operation principle of XRD is based on Bragg's Law [49]

1.6.2 Scanning Electron Microscopy

Scanning electron microscopy, popularly known as SEM, is an equipment that generates highly magnified pictures by using electrons as opposed to light, allowing researchers to study the morphology of the films on the molecular level. An electron gun that produces high-energy electron beams is placed at the microscope's top section. The beam passes across electromagnetic fields and lenses, in a high-vacuum environment, that concentrates the beam on the sample. Electrons and X-rays are emitted from the sample as a result of the beam strike. Then, detectors transform the emitted electrons and x-rays into a signal. Then the final picture is generated based on the signals [50]. Figure 13 illustrates the operating principle of SEM.

When the electrons collide with the material, they generate different types of signals that can be collected and used for measurements such as backscattered electrons, X-rays, and secondary electrons. Backscattered and secondary electrons are two well-known and crucial signals. Electrons that are reflected from the material via elastic scattering are known as Backscattered electrons whereas Secondary electrons, on the other hand, are a consequence of an inelastic collision. These signals are gathered by several detectors to generate pictures that are ultimately shown on the screen. Upon impact with the sample's surface, the electron beam penetrates the material for about a few microns. The penetration is directly dependent on the voltage and material density. Consequently, several signals, including secondary electrons, are generated [50].

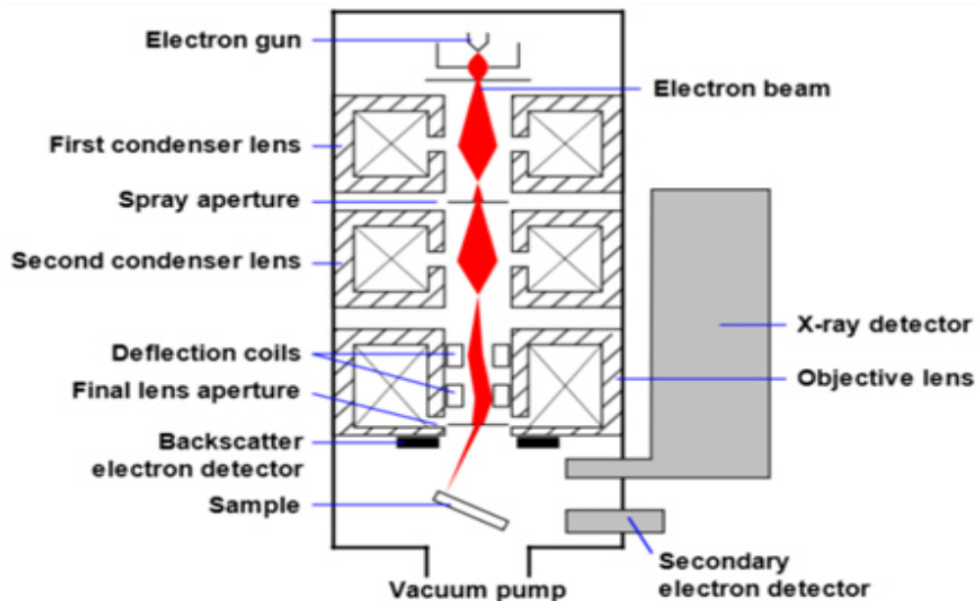


Figure 13. The operation principle of SEM [51]

1.6.3 UV-VIS Spectroscopy

UV-Vis Spectroscopy is a technique that permits the evaluation of the optical properties of a sample, including transmittance, reflectance, and absorbance by measuring and comparing the intensity of light traveling through a sample and a reference sample. The data may then be used to determine the absorbance as a proportion of the total quantity of light that passed through the sample. Visible light and ultraviolet light are often utilized as radiation intervals. From these optical measurements, the absorption coefficient, band gap, and thickness of the film can be estimated [52]. Figure 14 illustrates the measurement principles in UV-Vis spectroscopy.

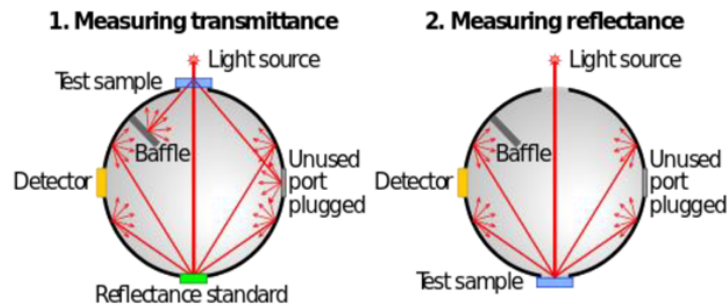


Figure 14. Principle of measurement of transmittance and reflectance UV-VIS Spectroscopy [53]

The absorption coefficient, α , can be determined using the data from the spectroscopy regarding transmittance and reflectance with the help of the equation below, where R is the percentage of light reflected, T is the percentage of light transmitted, and d is the thickness of the material [52]:

$$\alpha = \frac{1}{d} \ln\left(\frac{1-R}{T}\right) \quad (2)$$

1.7 Solar Cell Characterization Methods

1.7.1 Current Density-Voltage measurement (J-V)

Current density-voltage (J-V), is an accurate technique for measuring the efficiency and solar cell performance. To evaluate the efficiency of a solar cell, three important factors are required: short circuit current (J_{sc}), open circuit voltage (V_{oc}), and fill factor (FF). By monitoring these factors, we can compute the device's power conversion efficiency (PCE) using formula 3 [54]:

$$PCE = \frac{P_{out}}{P_{in}} = \frac{V_{oc} J_{sc} FF}{P_{in}} \quad (3)$$

P_{in} is the luminous power and it relies on the chosen illumination source. Thus, it is essential that the solar power simulator appropriately duplicate the sun spectrum [55]. These characteristics can be determined using current-voltage measurement. In this technique, the device is kept at a sequence of voltages, and the current density flowing through the device as a consequence of the voltage is measured. This measurement provides a J - V curve which can be used to determine the required parameters. Scientists typically use current density instead of merely current when analyzing solar cells, which enables them to compare devices with various active regions [54]. Figure 15 shows the J - V curve and highlights the important areas and points. The efficiency of a solar device can also be calculated according to equation 4, where V_{mp} and J_{mp} are the maximum power point voltage and current density respectively and P_{light} is the power of the illumination lamp:

$$\eta = \frac{V_{mp} J_{mp}}{P_{light}} \quad (4)$$

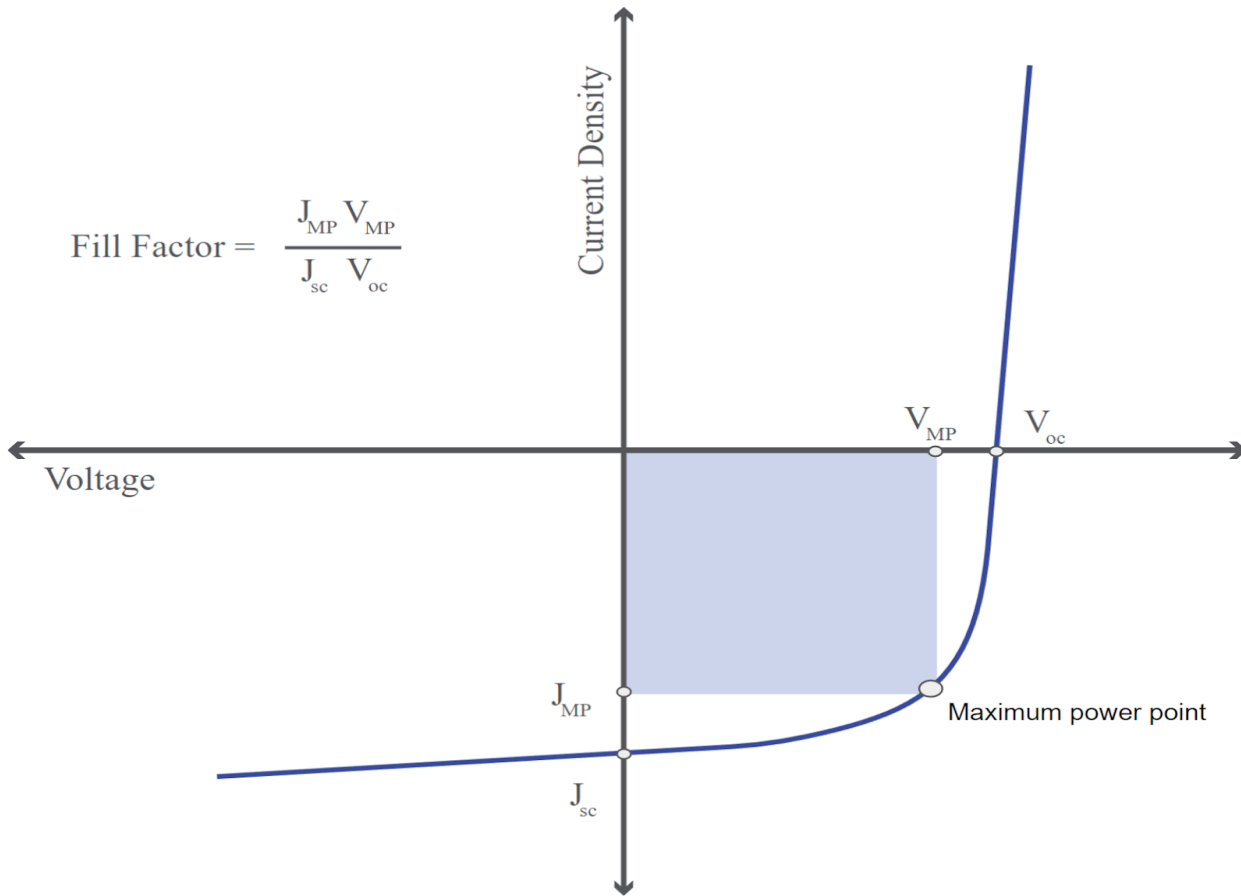


Figure 15. Current density-Voltage curve under illumination; V_{mp} is the maximum voltage in V, J_{mp} is the maximum current density in mA/cm², V_{oc} is the open-circuit voltage, and J_{sc} is the short-circuit current density [55]

1.7.2 External quantum efficiency (EQE)

External Quantum Efficiency (EQE) is the ratio of the number of charge carriers captured by solar cells to the number of incident photons. Quantum efficiency can be expressed as a function of either wavelength or energy. When all photons that have a specific wavelength are absorbed and the associated minority carriers are captured, the quantum efficiency at that wavelength is equal to one. Quantum efficiency is zero for photons with energies below the band gap. Quantum efficiency is idealized as a square, however, recombination factors diminish the quantum efficiency of the vast majority of solar cells. The same processes that impact the chance of collection also influence quantum efficiency. For instance, green light gets absorbed in the bulk of a solar cell, and a short diffusion length reduces the quantum efficiency in the green section of the

spectrum by affecting the likelihood of collection from the bulk of the solar cell. Figure 16 illustrates an example of a quantum efficiency curve [56].

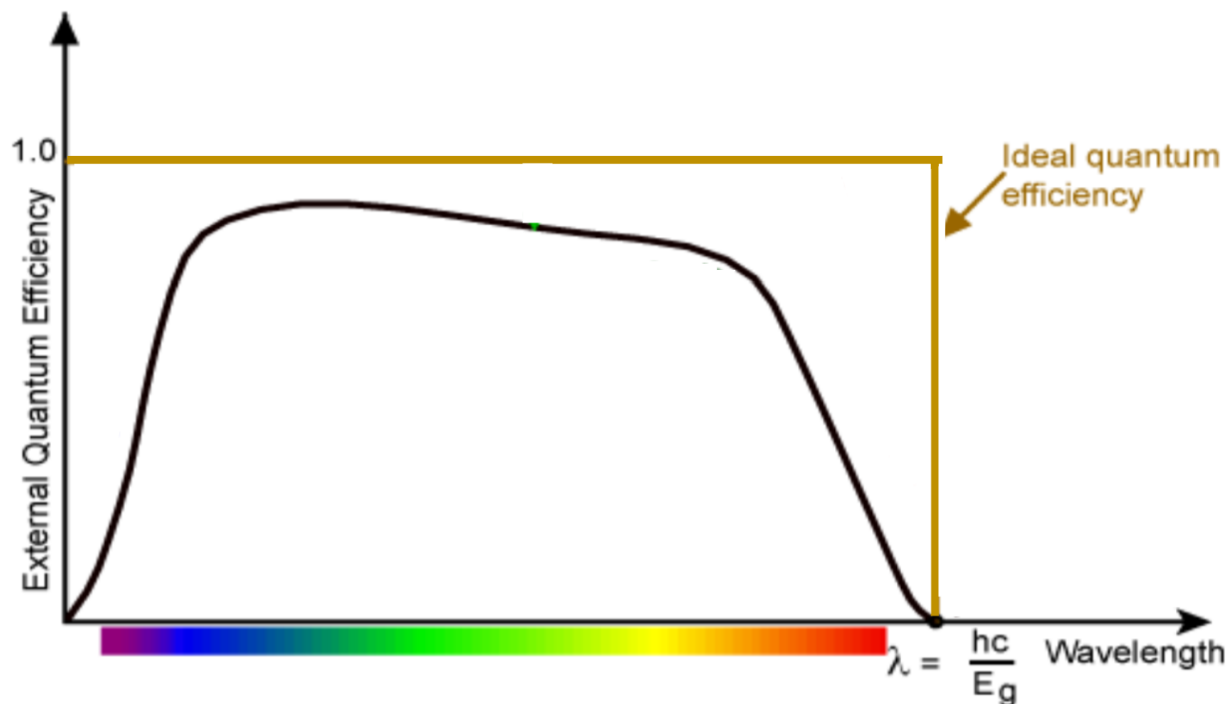


Figure 16. Typical quantum efficiency curve [56]

1.8 Summary of theoretical background and aims of the Thesis

According to the literature review, the following traits should be taken into account:

1. Titanium dioxide, commonly known as TiO_2 , is an n-type semiconductor with a wide band gap that has demonstrated value as the electron transport layer for Sb_2S_3 -based solar cells.
2. Antimony Sulfide is a non-toxic, promising, and well-known absorber material with a desirable band gap of between 1.7 and 1.8 eV. Scientists and researchers have spent countless hours researching, analyzing, and developing the Sb_2S_3 absorber layer over the past decade. Additionally, the combination of Sb_2S_3 absorber with various electron and hole transport materials has resulted in ever-increasing efficiencies. Recently, Wang et. al., has fabricated solar cells with solar cell configuration of FTO/CdS/ Sb_2S_3 /Spiro-OMeTAD/Au yielding PCE of 8.0%.
3. Ultrasonic spray pyrolysis and spin-coating are two of the most popular deposition methods for absorber Sb_2S_3 . In this work, the ultrasonic spray pyrolysis method was utilized to deposit a layer of Sb_2S_3 on a glass/FTO/ TiO_2 substrate.
4. P3HT is a well-known, low-bandgap polymer within organic photovoltaics studies. However, some challenges in utilizing P3HT as HTM in Sb_2S_3 -based solar cells are that they exhibit parasitic absorption and require an additional activation step.
5. Spiro-OMeTAD is a high-performance and another popular material used as a hole transport layer in Sb_2S_3 -based solar cells. Initially used as an HTM in perovskite solar cells (PSC) in 2012 and exhibited a remarkable 9.7% efficiency which attracted more and more interest over the years. Some of the disadvantages associated are its low stability even at temperatures as low as 100°C and the requirements of additional dopants.
6. P3HT and Spiro-OMeTAD are two popular HTMs used in Sb_2S_3 -based solar cells. However, there are only a handful of papers where a direct comparison between the impact of these two HTMs on Sb_2S_3 solar cell performance is studied.
7. Spiro-OMeTAD is a well-known HTM material in perovskite solar cells, but to attain the maximum PCE in Sb_2S_3 solar cells, it is crucial to determine its ideal layer thickness.

Based on the previous points, the following objectives could be outlined for the following thesis:

1. To successfully fabricate Sb_2S_3 solar cells by using ultrasonic spray pyrolysis to deposit electron transport layer - TiO_2 and absorber - Sb_2S_3 .
2. To deposit P3HT and Spiro-OMeTAD as HTMs using spin coating.
3. Morphological, optical, and electrical characterization of the fabricated solar cells using SEM, XRD, UV-VIS, J-V, and EQE measurements.
4. To study the impact of the HTM layer thickness on the solar cell performance, by employing a systematic approach in which the thickness is optimized by changing the concentration of the HTM precursor solution.
5. To compare the performance of the solar cells targeting semitransparency with HTMs - P3HT and optimized Spiro-OMeTAD.

2. EXPERIMENTAL

In this study, three sets of samples were fabricated to study the optoelectrical properties of the solar cell prepared with two different HTMs - P3HT and Spiro-OMeTAD. The first set consisted of structure glass/FTO/TiO₂/Sb₂S₃/HTM, where the HTM was P3HT or Spiro-OMeTAD. This configuration was used for characterization techniques like XRD and UV-VIS. The second set consisted of structure glass/FTO/TiO₂/Sb₂S₃/HTM with P3HT or Spiro-OMeTAD/Au as the HTMs. This set was utilized for electrical characterization methods such as J-V and EQE measurements. The third set with structure Glass/FTO/HTM was used to measure the optical properties of the HTM layers.

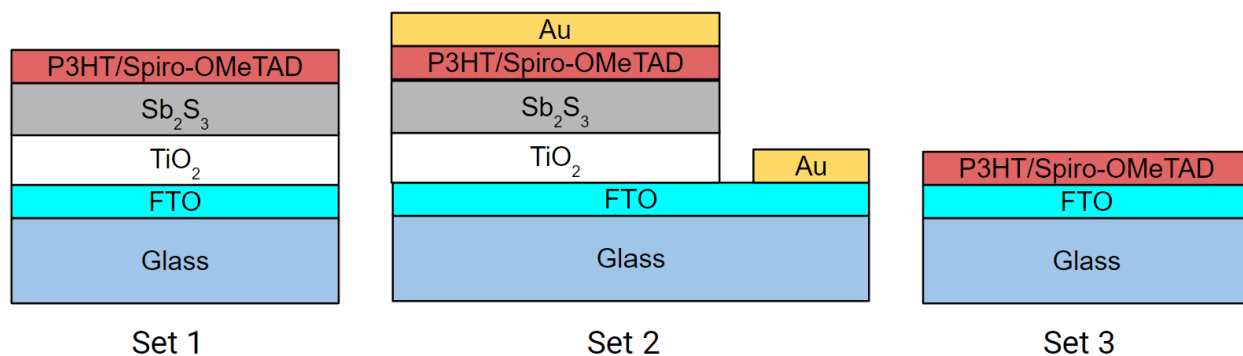


Figure 17. Principal structures of the three sets of samples prepared

2.1 Fabrication of solar Cell

2.1.1 Cleaning and Preparation of substrate (Glass/FTO)

Sigma-Aldrich's FTO-coated glass with a thickness of 2.3 mm and surface resistivity of 7 Ω/sq, was employed as the substrate.

The FTO-coated glass substrate was sliced into 18x18 mm squares. The cleaning procedure includes boiling the FTO substrates in distilled water for 5 minutes. After cooling it down the substrates were rinsed in methanol and dried at room temperature. Then immediately these samples were transferred to the hot plate at 120°C for removal of the remaining solvents.

2.1.2 Deposition of the Electron Transport Layer (TiO₂) by ultrasonic spray pyrolysis

Ultrasonic spray pyrolysis (USP) was used to deposit a layer of TiO₂ on the FTO-coated glass substrate. Initially, the temperature of the hot plate was set to 120°C. Once all the samples were placed on the hot plate, the temperature was raised to the deposition temperature of 360°C.

To prepare a precursor solution of 100 mL with 0.1 M concentration, 5.7 mL of titanium (IV) isopropoxide (TTIP) and 2 mL of acetylacetonate (AcAc) [C₅H₈O₂], were added to 92.3 mL of ethanol. The mixed amounts were based on a molecular weight ratio of 1:1 for TTIP to AcAc. The standardized deposition technique provides a layer thickness of 80-100 nm [30] [57] [58]. Before the start of the deposition, the hot plate surface, reactor, and tube transferring the precursor solution were all washed with ethanol and then dried. With the deposition temperature of 360°C, 75 cycles of deposition, and a carrier gas flow rate of 7 mL/min, a total of eight samples were prepared. The deposition lasted approximately 37 minutes and required 75 mL of the precursor solution. After deposition, the films were annealed at 450°C on the hot plate in ambient air for 30 minutes. Finally, the samples were cooled for 15 to 20 minutes. Figure 18 shows the annealed TiO₂ samples.



Figure 18. TiO₂ deposited and annealed samples on glass/FTO substrate.
Structure: glass/FTO/TiO₂/Sb₂S₃

2.1.3 Deposition of the absorber (Sb_2S_3) by ultrasonic spray pyrolysis

Before starting the deposition process, the hot plate surface, ultrasonic reactor, and precursor transferring tube were cleaned and dried with ethanol.

Since the Sb_2S_3 precursor solution is susceptible to the presence of moisture, an additional cleaning step with methanol was performed on all the equipment, including those previously mentioned, to remove any moisture that may have remained after the initial cleaning step.

120 mL of precursor solution was prepared by dissolving 1.644 grams of Thiourea ($\text{CH}_4\text{N}_2\text{S}$) and 7.2 mL of Antimony trichloride (SbCl_3), in 112.8 mL of methanol. The deposition process was performed under the following conditions: 40 deposition cycles, deposition temperature of 198°C , and a carrier gas flow rate of 7 mL/min. 80 mL of the precursor solution was consumed in the deposition process. Next, the as-deposited samples were crystallized by hot plate annealing in N_2 environment. The crystallization procedure consisted of three stages: 90 seconds under N_2 flow, 6 minutes of heating in N_2 at 170°C on a hot plate, and then an additional 90 seconds under N_2 flow to cool down the samples. Figure 19 illustrates the samples in different stages of the crystallization process.

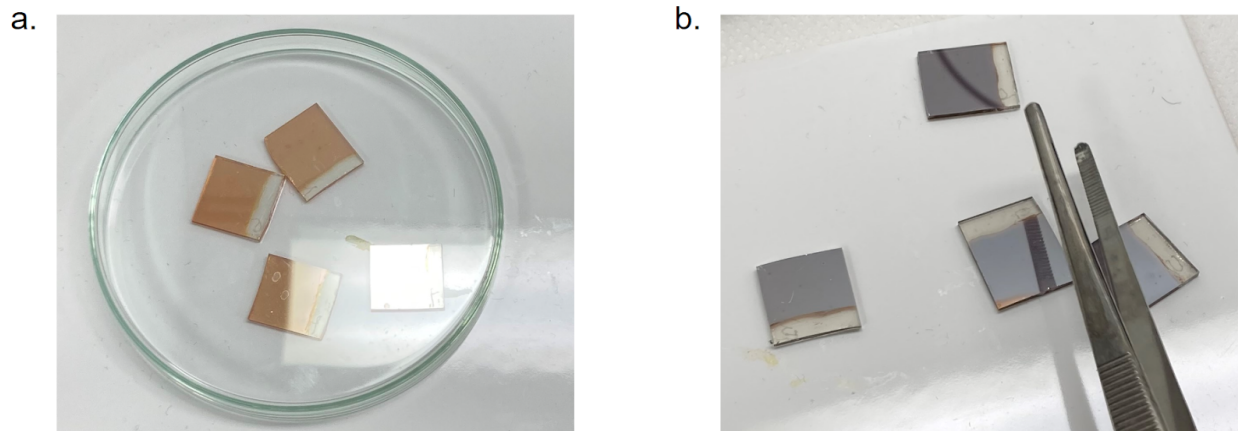


Figure 19. Sb_2S_3 samples during different stages of crystallization **a)** As deposited Sb_2S_3 samples and **b)** Sb_2S_3 samples after annealing in N_2 .

Structure: glass/FTO/ TiO_2 / Sb_2S_3

2.1.4 Spiro-OMeTAD precursor preparation and deposition by spin coating

The precursor solution was prepared by dissolving 70 mg of as received powder of Spiro-OMeTAD in 1 mL of chlorobenzene (C₆H₅Cl). This was followed by the addition of dopants. 10 μL of FK 209 Co(III) TFSI salt with chemical formula C₄₂H₄₅CoF₁₈O₁₂N₁₂S₆, 5 μL of Lithium bis(trifluoromethanesulfonyl)imide or LiTFSI with chemical formula LiC₂NO₄F₆S₂, and 20 μL of Tributyl phosphate or TBP with chemical formula C₁₂H₂₇O₄P were added.

To examine the impact of Spiro-OMeTAD concentration on solar cell performance, three solutions with varying ratios of Spiro-OMeTAD to chlorobenzene were prepared. The initial solution, referred to in this experiment as Spiro1x (60mM), was diluted two and four times to prepare Spiro2x and Spiro4x. Spiro2x (30mM) was prepared by mixing 200 μL of the precursor solution with 200 μL of chlorobenzenes in a 1:1 ratio. The third solution, Spiro4x (15mM) was prepared by mixing 100 μL of the precursor solution with 300 μL of chlorobenzene, resulting in a 1:3 ratio. The three concentrations of the precursor solutions are referred to throughout this study as Spiro1x, Spiro2x, and Spiro4x.

Spiro1x - 60 mM

Spiro2x - 30mM

Spiro4x - 15mM

The deposition process was conducted by using the spin coating method at 3000 rpm for 30 seconds. No additional post-deposition treatment step was utilized after the completion of deposition in the case of HTM Spiro-OMeTAD.

2.1.5 P3HT precursor preparation and deposition by spin coating

To prepare the P3HT precursor solution, 11 mg of as received powder was dissolved in 1 mL of chlorobenzene and then mixed for 30 minutes using a magnetic stirrer. This was followed by the spin-coating deposition process at 3000 rpm for 20 seconds. Upon completion of the deposition of the P3HT layer, an additional post-deposition treatment was applied to rearrange the molecules and activate the P3HT layer. The complete process consists of three sub-steps. Initially, the sample was exposed to N₂ flow for 90 seconds, then it was placed on a hot plate at 170°C for 5 minutes, and finally, it was cooled in N₂ for another 90 seconds.

2.1.6 Deposition of metal contacts by thermal evaporation

The solar cells fabrication step was completed by depositing gold contacts using a metal mask onto the structure glass/FTO/TiO₂/Sb₂S₃/HTM using thermal evaporation. The resulting active area of the solar cells was 7.06 mm². After the deposition was completed, samples were allowed to cool down in the vacuum chamber before being removed and prepared for measurements. The schematic of the complete fabrication process of solar cells is shown in Figure 20.

2.2 Material characterization

In Sb₂S₃-based solar cells, the quality of the underlying absorber film – Sb₂S₃ is critical to obtain solar cells with good performance. Therefore, it becomes essential to ascertain the quality of films prior to their suitability for application in solar cells. In order to examine the structural and phase constitution of the as-deposited and annealed Sb₂S₃ films, characterization by X-ray diffraction (XRD) was performed using a Rigaku Ultima IV instrument equipped with a Cu K_α source ($\lambda = 1.5406 \text{ \AA}$) over a 2θ range of 10–80° with a step size of 0.02° [59]. The following data cards were utilized to examine XRD patterns using Rigaku PDXL software:

- ICDD PDF 00-041-1445 for FTO
- ICDD PDF 00-064-0863 for TiO₂
- ICDD PDF 01-075-4013 for Sb₂S₃

2.3 Solar cell characterization

To evaluate the J-V characteristic, AUTOLAB PGSTAT 30 and an Oriel class A solar simulator 91159A (100 mW cm⁻², AM1.5) were employed. A 300 W xenon lamp and an SPM-2 Carl Zeiss-Jena monochromator at 30 Hz were utilized for EQE measurement [80]. The cross-sectional morphologies of the layers were recorded by Zeiss HR FESEM Ultra 55 (SEM) at an electron beam accelerating voltage of 4 kV. Using a Jasco V-670 ultraviolet-visible (UV-VIS) spectrophotometer, the 300-1500 nm wavelength region of UV-VIS characterization was measured. The transmittance and reflectance percentages of the light source were determined using this method, and the absorption percentage was calculated and graphed using these results.

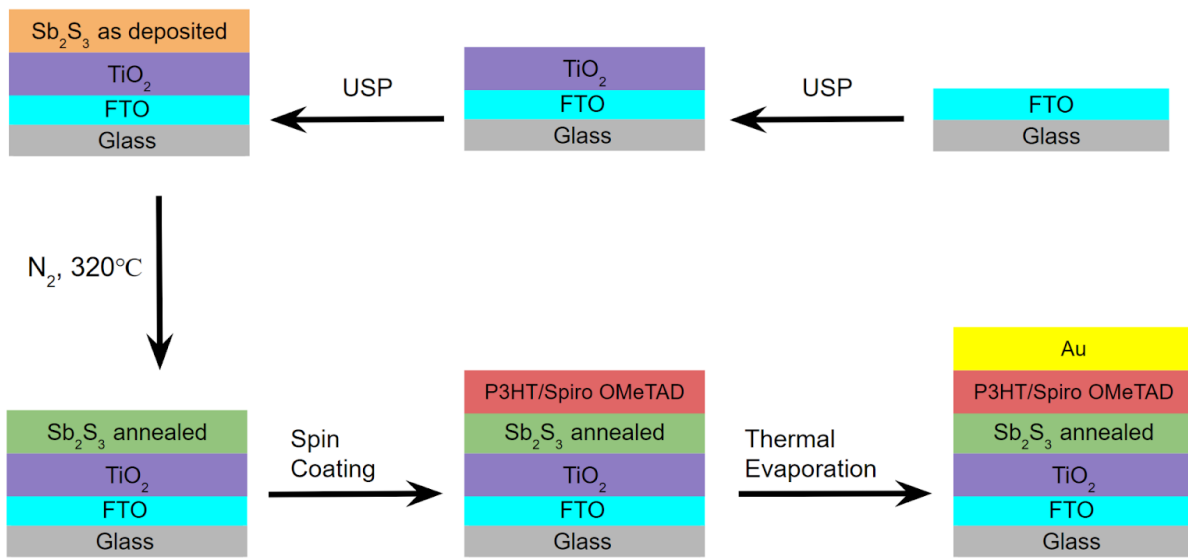


Figure 20. Schematic of the preparation procedure adopted for the fabrication of Sb₂S₃ solar cells.

3. RESULTS AND DISCUSSION

3.1 Structural properties of Sb_2S_3 films

The surface of the as-deposited and annealed Sb_2S_3 films is analyzed using optical microscopy and the resulting images are shown in Figure 21. As evident from the images, the surface of the substrates is uniformly covered with amorphous Sb_2S_3 films, and the annealed films exhibit grain structure. Annealing Sb_2S_3 films has resulted in a visible color change, with orange-colored as-deposited films becoming dark brown after annealing as seen in Figure 22.

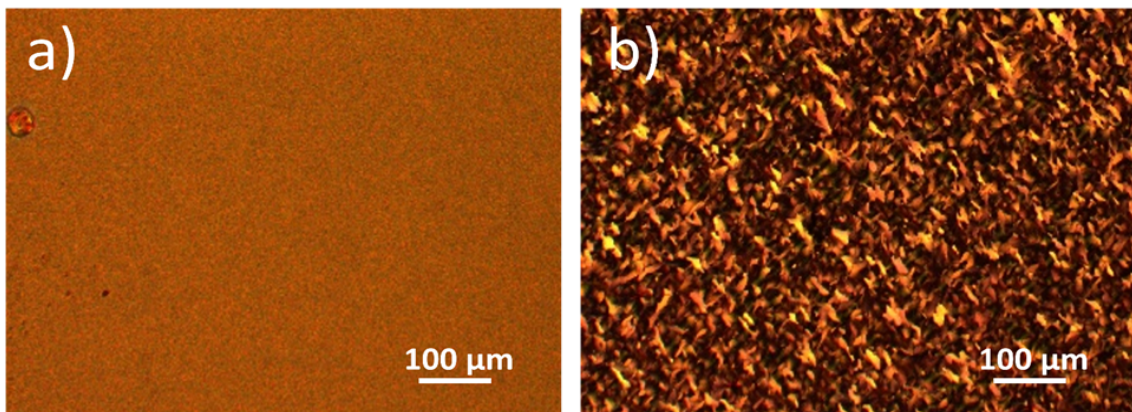


Figure 21. Optical microscope images of the surface of **a)** as-deposited and **b)** annealed Sb_2S_3 solar cells

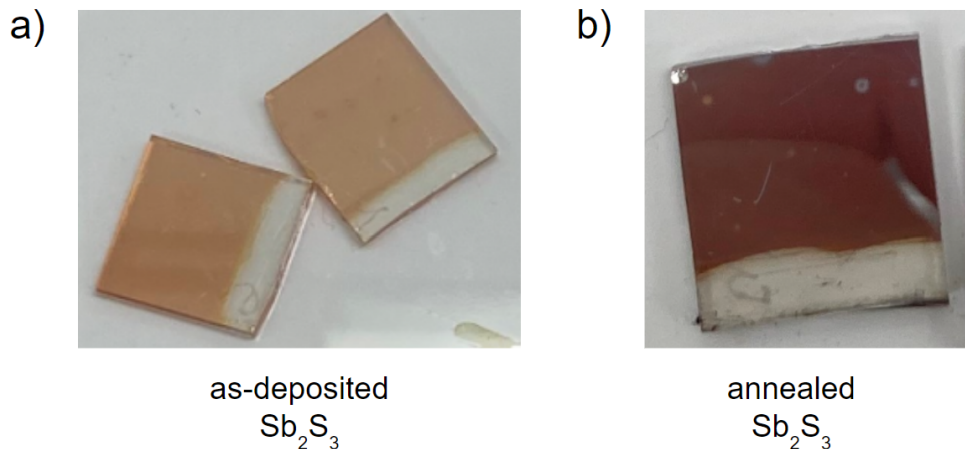


Figure 22. Change in color of Sb_2S_3 thin films as a result of the annealing; **a)** as deposited Sb_2S_3 films and **b)** annealed Sb_2S_3 films.

Figure 23 shows the XRD patterns of the as-deposited and annealed Sb_2S_3 films. The XRD pattern of the sample with the as-deposited Sb_2S_3 film reveals the peaks belonging to the FTO and TiO_2 layers. The XRD pattern belonging to the annealed Sb_2S_3 film shows sharp Stibnite structure peaks at 2θ of 15.9, 17.8, 29.2, and 30.5° which agree with the previous reports [30] [57] [58]. The measurement suggests that the as-deposited Sb_2S_3 films are amorphous. After annealing in N_2 environment, the resulting Sb_2S_3 films are completely crystallized. No oxide peaks of Sb_2O_3 are detected at 2θ of 13.6 and 27.5° [30], which signals that the annealed Sb_2S_3 films are of high quality without any undesirable impurities. The morphological, structural, and optical analyses of annealed Sb_2S_3 films indicate that the prepared absorber layer covers the ETL (TiO_2) layer conformally and has a single stibnite phase which is desired for solar cell applications.

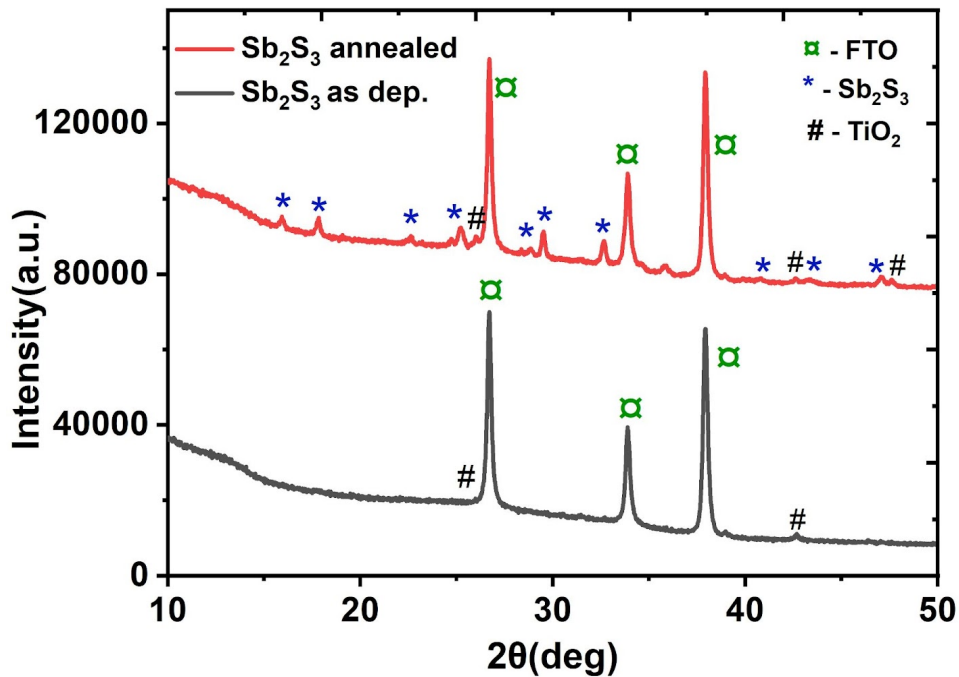


Figure 23. XRD patterns of the as-deposited and annealed Sb_2S_3 films

3.2 Application of HTMs in solar cells

3.2.1 Electrical Characterization

Glass/FTO/TiO₂/Sb₂S₃/HTM/Au configuration was used to fabricate thin-film Sb₂S₃-based solar cells. On the crystallized Sb₂S₃ absorber, P3HT and Spiro-OMeTAD are spin coated followed by the thermal evaporation of Au to complete the solar cell fabrication. The current density–voltage (J–V) characteristics of the fabricated solar cell devices are measured under one sun illumination (AM 1.5G) and the J–V curves of the champion cells for each device are shown. As seen from previous studies, P3HT–1 wt.% results in a thickness of 80 nm, which is the highest solar cell efficiency out of all studied concentrations (0.5, 1, and 2 wt.%) [30] as shown in Figure 24 and the solar cells performance parameters are summarized in Table 2.

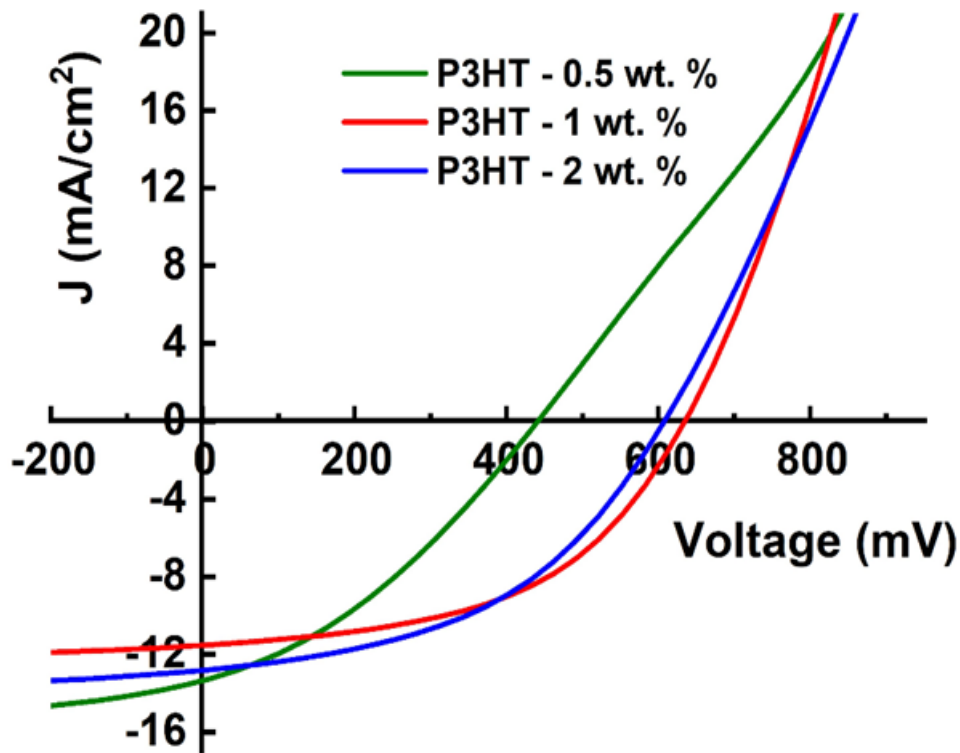


Figure 24. J–V curves of the top-performing Sb₂S₃ solar cells with different concentrations of P3HT as HTM (0.5, 1, and 2 wt. %). Structure: glass/FTO/TiO₂/Sb₂S₃/P3HT/Au [30].

Table 2. Device parameters of Sb_2S_3 solar cells with 0.5, 1, and 2 wt. % of P3HT [30].

Device with P3HT concentration (wt. %)	V_{OC} (mV)	J_{SC} (mA/cm ²)	FF (%)	PCE (%)
0.5	441	13.2	35	2.0
1	634	11.5	50	3.7
2	608	12.8	46	3.6

To use Spiro-OMeTAD as an HTM in Sb_2S_3 -type solar cells, it is necessary to determine the precursor solution concentration in order to obtain a layer of appropriate thickness for efficient solar cells. Changing the HTM concentration of the solution is the factor that allowed us to alter the layer thickness.

The current density–voltage curves of the champion cells along with a summary of the corresponding photovoltaic parameters are shown in Figure 25 and Table 3, respectively. According to the J-V characteristics, the cell output is very low when using the Spiro1x solution. A reasonable V_{OC} value of 578 mV indicates that the desired p-n junction was formed and the low PCE value of 0.03% is due to a low J_{SC} of 0.2 mA/cm². The extremely low J_{SC} of the solar cell could be attributed to the larger series resistance (R_s), which also results in very low FF. The larger R_s is mainly due to the relatively thick HTM layer which resulted in the series resistance of the Spiro1x solar cell device to be 170.6 $\Omega\text{-cm}^2$. Further, the precursor solution was diluted from 60 mM (Spiro1x) to 30 mM (Spiro2x). Diluting the HTM solution resulted in the fabricated solar cell device achieving higher J_{SC} and V_{OC} . V_{OC} rose from 578 mV to 581 mV, J_{SC} rose from 0.20 to 3.52 mA/cm², and PCE rose from 0.03 to 0.5% when the concentration of Spiro-OMeTAD was decreased from 60 to 30 mM. A thinner HTM layer is expected while diluting the HTM solution. This is observed as the R_s of the solar cell device show a sharp decrease from 170.6 to 4.2 $\Omega\text{-cm}^2$ when the HTM solution is diluted 2 times. Further dilution to 15 mM (Spiro4x) yielded solar cells with V_{OC} values of 653 mV, J_{SC} value of 11.7 mA/cm², and PCE values of 3.12%. Upon dilution, the R_s of the solar cell

device decreased from 4.2 to 0.98 $\Omega\text{-cm}^2$. A correlation between the concentration of Spiro-OMeTAD precursor solution and the solar cell output is observed. According to the obtained solar cell parameters, it can be concluded that lower concentrations of HTM Spiro-OMeTAD solution resulted in significantly lower values for R_s while considerably higher J_{sc} and resulting PCE.

Further, for a fair comparison of Spiro-OMeTAD as the HTM, the optimized solar cells with 15 mM concentration are compared with the devices made using P3HT as HTM. The concentration of P3HT (0.5, 1, and 2 wt. %) has been optimized as described earlier and shown in Figure 24, which shows that solar cells with 1 wt. % P3HT has yielded the highest PCE and is therefore used as a reference. Champion solar cells with P3HT exhibited a V_{oc} value of 645 mV, J_{sc} value of 11.9 mA/cm^2 , fill factor (FF) of 50%, and PCE values of 3.9%. In comparison with Spiro4x, solar cells with P3HT as HTM yielded similar V_{oc} and J_{sc} but higher FF. A lower FF in the case of devices with Spiro-OMeTAD is a result of higher charge carrier recombination at the absorber/HTM interface.

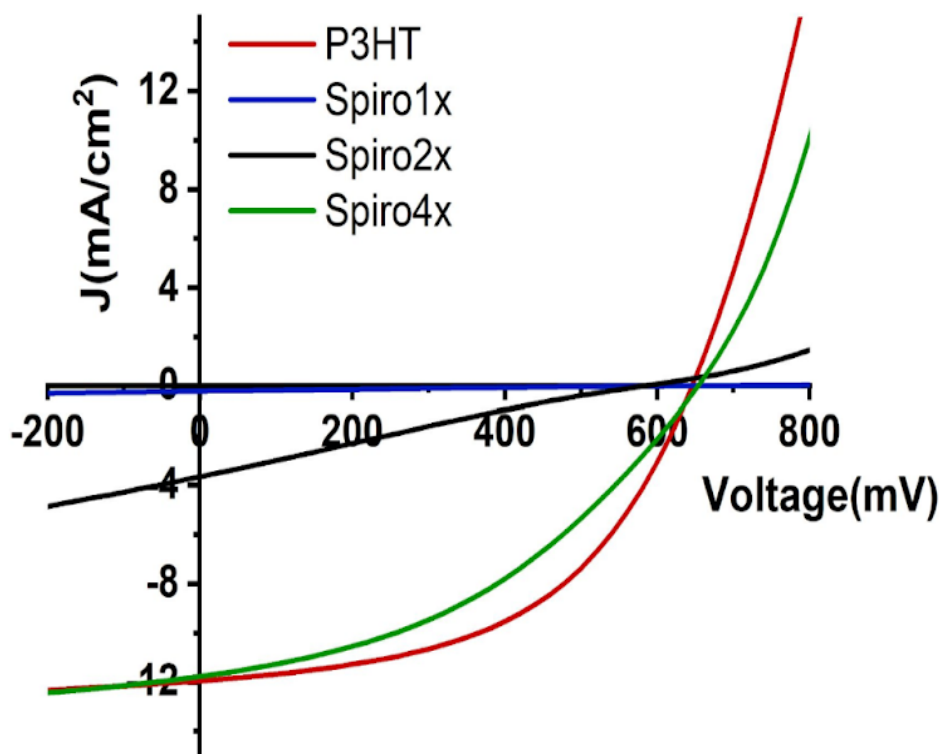


Figure 25. J-V curves of the champion Sb_2S_3 solar cells P3HT, Spiro1x, Spiro2x, and Spiro4x HTMs.

Table 3. Device parameters of the top-performing Sb_2S_3 solar cells with HTMs - P3HT, Spiro1x, Spiro2x, and Spiro4x.

HTM	HTM conc. (mM)	V_{oc} (mV)	J_{sc} (mA/cm ²)	FF (%)	PCE (%)	R_s ($\Omega\cdot\text{cm}^2$)
P3HT	1 wt. %	645	11.9	50	3.9	0.87
Spiro1x	60	578	0.20	24	0.03	170.60
Spiro2x	30	581	3.52	23	0.50	4.20
Spiro4x	15	653	11.7	41	3.12	0.98

Cross-sectional images of solar cell stacks with optimized Spiro-OMeTAD and P3HT are shown in Figure 26a and Figure 26b, respectively. The thickness of the Electron transport layer TiO_2 is ca. 90 nm while the absorber layer Sb_2S_3 is ca. 80 nm. The optimized Spiro4x is a considerably thinner layer (ca. 20-25 nm) compared to the P3HT (ca. 100 nm). It is important to note that the Spiro4x and P3HT are independently optimized for the Sb_2S_3 solar cell stack. This shows that a thinner Spiro-OMeTAD is sufficient for obtaining solar cells with comparable efficiency to P3HT.

The external quantum efficiency (EQE) curves of the fabricated Sb_2S_3 solar cell devices with the different HTMs are presented in Figure 27. EQE of devices with P3HT and varied concentrations of Spiro-OMeTAD (Spiro1x, Spiro2x, and Spiro4x) was measured and analyzed. As seen previously from the JV curves, the EQE spectral response in the case of devices with HTM Spiro1x is very low. Similarly, the EQE response for devices with Spiro4x is higher than that of Spiro2x. The result indicates that there is a correlation between Spiro-OMeTAD concentration and EQE response; lower Spiro-OMeTAD concentrations have resulted in a greater EQE response. In consequence, among the Spiro-series HTMs, solar cells with Spiro4x exhibited the highest response.

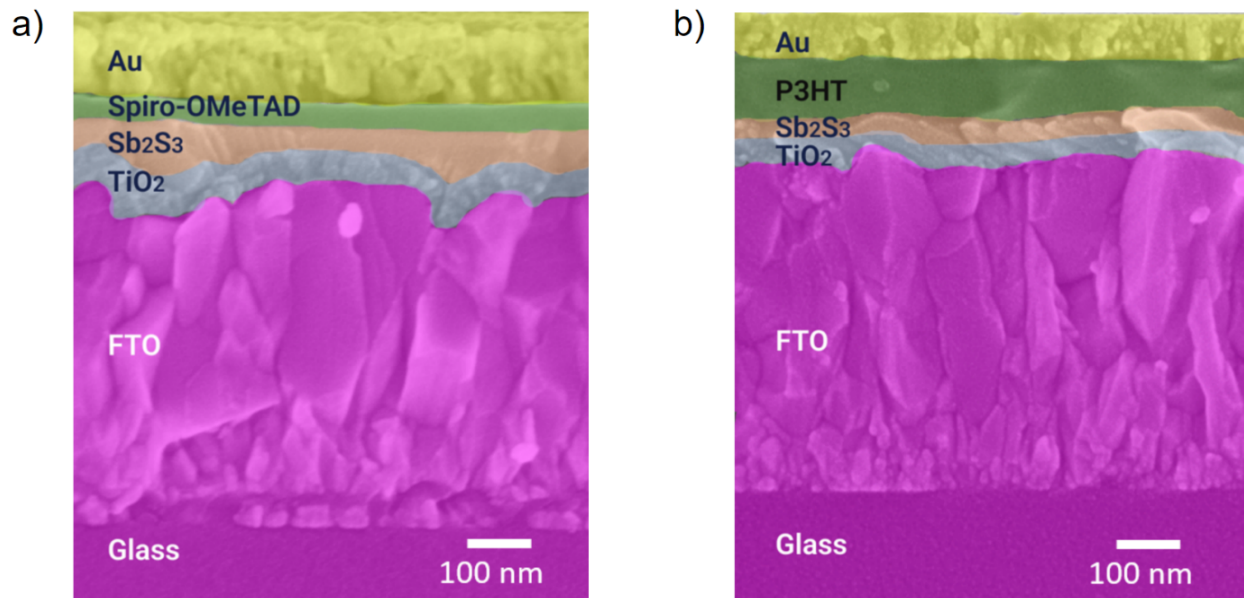


Figure 26. Cross-sectional SEM images of glass/FTO/TiO₂/Sb₂S₃/HTM/Au solar cells with **a)** Spiro4x and **b)** P3HT as the HTM. Spiro4x is a significantly thinner layer (ca. 25 nm) than P3HT (ca. 100 nm).

In comparison, EQE response for the solar cell with P3HT is consistently higher than that of the solar cell with Spiro4x between 300 and 500 nm, but a concavity in the EQE curve is observed for the solar cell with P3HT in the range of 500-700 nm, which is absent in the EQE graphs of solar cells with Spiro4x.

It is known from studies that P3HT absorbs majorly in the 500-600 nm region due to its bandgap at 1.8 eV [30] [57] [58], thus attributing it to parasitic absorption [23]. The parasitic absorption losses coupled with absorption in the visible range exhibited by P3HT are not present in the case of Spiro-OMeTAD. A higher spectral response validates the efficacy of Spiro-OMeTAD as HTMs for semi-transparent solar cells.

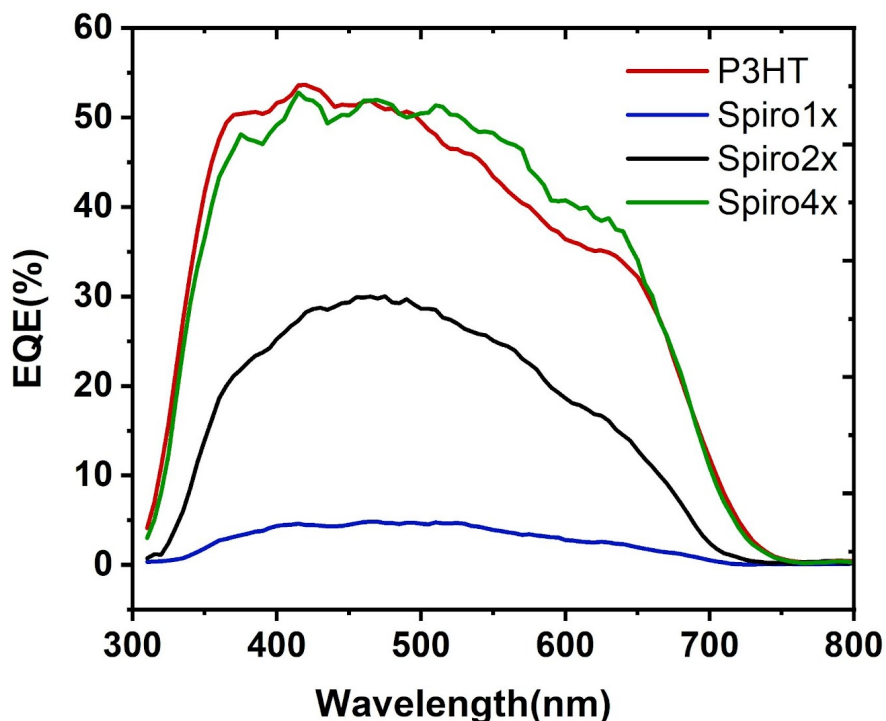


Figure 27. EQE spectral response of Sb_2S_3 solar cells with HTMs - P3HT and different concentrations of Spiro-OMeTAD.

3.2.2 Optical Characterization

Figure 28a shows the measured transmittance spectra of HTM layers - P3HT, Spiro1x, Spiro2x, and Spiro4x deposited on glass/FTO substrate. The transmittance spectra of layers - Spiro1x, Spiro2x, and Spiro4x are nearly identical from 450 to 800 nm. However, at approximately 430 nm, the transmittance spectra begin to diverge due to absorption differences and a decrease in the transmittance of the HTMs mainly due to their thicknesses. In the range of 300 to 430 nm, Spiro4x, Spiro2x, and Spiro1x exhibit the highest transmittance and lowest absorbance, respectively. In comparison - P3HT, on the other hand, exhibits parasitic absorption in the range of 400 - 650 nm as indicated by a steep drop in this range. Unlike P3HT, samples coated with Spiro1x, Spiro2x, and Spiro4x do not exhibit this dip. Figure 28b illustrates the calculated average visible transmittance (AVT) values in the 380-800 nm region for all the HTM layers. It is seen that AVT for P3HT is around 65% and for Spiro1x, Spiro2x, and Spiro4x is around 75%.

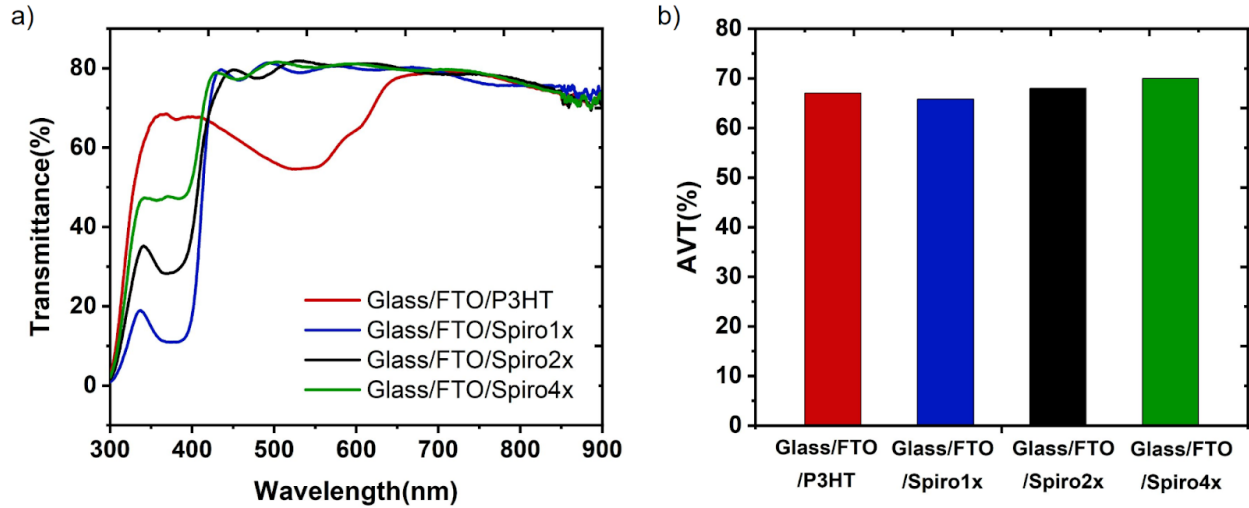


Figure 28. Total transmission spectra of **a)** P3HT, Spiro1x, Spiro2x, and Spiro4x layers on glass/FTO substrate and **b)** Respective average visible transmittance bar charts of the HTM films in 380-800 nm range.
Structure: glass/FTO/ HTM

Next, transmittance was calculated for the solar cell stack devoid of metal contact (glass/FTO/TiO₂/Sb₂S₃/HTM) as shown in Figure 29a. The calculated AVT of the devices are shown in Figure 29b. AVT of solar cell devices with Spiro-OMetad as HTMs exceeded 20%, whereas the AVT of the device with P3HT as HTM is approximately 18%. The AVT of the devices with Spiro1x and Spiro4x HTMs was approximately 22%, while the AVT of the device with Spiro2x HTM was the highest of all HTMs at 25%. The enhancement of device-level transparency by 25% further validates the utilization of optimized concentration of Spiro-OMetad as HTM in semi-transparent Sb₂S₃ solar cells.

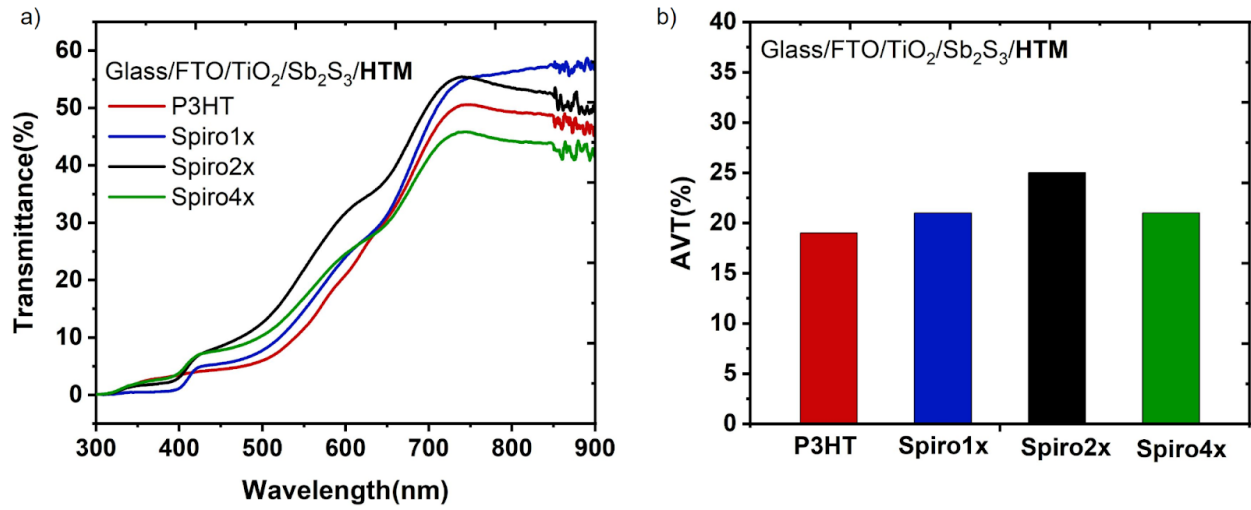


Figure 29. Total transmission spectra of **a)** solar cells with HTMs (P3HT, Spiro1x, Spiro2x, and Spiro4x) devoid of metal contact. **b)** Respective average visible transmittance bar charts of the solar cells in the 380-800 nm range.
Structure: glass/FTO/TiO₂/Sb₂S₃/HTM

CONCLUSION

The present study focuses on two commonly employed hole-transporting materials (HTMs) in Sb_2S_3 solar cells, namely Spiro-OMeTAD and P3HT. Solar cells were fabricated in the configuration - glass/FTO/ TiO_2 / Sb_2S_3 /HTM/Au. For the P3HT layer, a precursor solution containing 1 wt.% P3HT was used, as previous studies showed that this concentration was the most effective among 0.5, 1, and 2 wt.%. For the Spiro-OMeTAD layer, a systematic approach was used in which the thickness is optimized by changing the concentration of the HTM precursor solution. Three different precursor solutions with concentrations of 60, 30, and 15 mM were prepared in chlorobenzene solvent. The objective of this approach was to analyze (1) the structural and optical characteristics using SEM, XRD, and UV-vis spectroscopy and (2) to perform electrical characterization of the fabricated solar cell devices using J-V and EQE measurements.

The findings of the investigation are presented as follows:

1. J-V curve and EQE results confirmed that the concentration of Spiro-OMeTAD has a discernible effect on solar cell performance. The dilution of precursor solutions led to a lower R_s and higher J_{SC} and PCE for the devices. Solar cells with HTMs – Spiro1x (60 mM), Spiro2x (30 mM), and Spiro4x (15 mM) yielded PCE of 0.03, 0.5 and 3.1%, respectively.
2. Solar cell device with P3HT (1 wt.%) as HTM yielded a PCE of 3.9%, with V_{OC} of 645 mV, J_{SC} of 11.9 mA/cm^2 , and FF of 0.5. Whereas solar cell device with optimized Spiro4x (15 mM) concentration yielded a PCE of 3.1%, with V_{OC} of 653 mV, J_{SC} of 11.7 mA/cm^2 , and a FF of 0.4 which is lower than that of the device with P3HT.
3. Based on transmittance values and calculated AVT of HTM thin films, it was observed that the precursor concentration of Spiro-OMeTAD has a significant influence on the thickness of the HTM layer. This subsequently affects the percentage of source light transmitted through the layer; lower precursor concentrations led to a higher percentage of transmittance.
4. Solar cell with the P3HT as HTM has an AVT of 18%, and Spiro-OMeTAD exhibits an AVT of 25% in the spectral region 400-800 nm. As compared to P3HT devices, the transparency of the solar cell stack with optimized Spiro-OMeTAD is higher by over 20%.

In summary, the present research underscores the importance of selecting a suitable HTM, as it can substantially affect both the performance of the solar cell and its overall transparency. The findings of this investigation provide novel insights into the development of semi-transparent solar cells based on Sb_2S_3 that incorporate two widely employed HTMs, namely P3HT and Spiro-OMeTAD.

SUMMARY

The world's reliance on finite fossil fuels for energy has led to a worsening energy crisis. Even if there were an infinite supply of fossil fuels, the associated greenhouse gas emissions and global warming would still be significant concerns. To address this, finding sustainable long-term energy solutions is crucial. Photovoltaic Technology (PV) offers a promising alternative by converting solar energy into electricity without harming the environment. While silicon-based solar cells have dominated the market, the high manufacturing cost has spurred the search for alternative options. Thin-film solar cells, particularly those with an Sb_2S_3 absorber layer, are considered a viable alternative

This study focuses on the HTM layer in Sb_2S_3 -based solar cells with the aim of investigating the applicability of Spiro-OMeTAD as HTMs in Sb_2S_3 -based semi-transparent solar cells and comparing its performance to P3HT.

The recorded PCE of the fabricated solar cells containing HTMs – Spiro1x (60 mM), Spiro2x (30 mM), Spiro4x (15 mM), and P3HT (1 wt.%) were 0.03, 0.5%, 3.1%, and 3.9%, respectively. J-V, EQE, transmittance, and AVT measurements confirmed that the concentration of Spiro-OMeTAD precursor solution can dramatically alter the thickness of the HTM layer and ultimately has a substantial effect on the performance and transparency of the solar cell. Lower J_{sc} and FF values restrict the performance of solar cell with Spiro4x (15mM) compared to the solar cells with P3HT. However we found that a significantly thinner layer of Spiro4x (25 nm) is enough to achieve a PCE comparable to that of P3HT (100 nm).

There are still many improvements that were beyond the scope of this work due to the research budget and time constraints. The next step in this process is to determine the optimal concentration of Spiro-OMeTAD precursors, which ultimately determines the HTM layer thickness and solar cell PCE. Once this task has been completed, further optimization is needed in the deposition parameters of SpiroOMeTAD. The solar cell has to be fabricated for each parameter change and its results has to be compared with the solar cells with other commonly used HTMs.

REFERENCES

- [1] Ncei., M. I. (n.d.). Annual 2021 Global Climate Report. Retrieved December 26, 2022, from <https://www.ncdc.noaa.gov/sotc/global/202113>
- [2] Panwar, N. L., Kaushik, S. C., & Kothari, S. (2011). Role of renewable energy sources in environmental protection: A review. *Renewable and Sustainable Energy Reviews*, 15(3), 1513–1524. <https://doi.org/10.1016/j.rser.2010.11.037>
- [3] Lewis, N. S. (2007). Toward cost-effective solar energy use. *Science*, 315(5813), 798–801. <https://doi.org/10.1126/science.1137014>
- [4] Schlamadinger, B., Apps, M., Bohlin, F., Gustavsson, L., Jungmeier, G., Marland, G., Pingoud, K., & Savolainen, I. (1997). Towards a standard methodology for greenhouse gas balances of bioenergy systems in comparison with fossil energy systems. *Biomass and Bioenergy*, 13(6), 359–375. [https://doi.org/10.1016/S0961-9534\(97\)10032-0](https://doi.org/10.1016/S0961-9534(97)10032-0)
- [5] Armaroli, N., & Balzani, V. (2007). The future of energy supply: Challenges and opportunities. *Angewandte Chemie*, 46(1-2), 52–66. <https://doi.org/10.1002/anie.200602373>
- [6] Löff, G. O. G., Duffie, J. A., & Smith, C. O. (1966). World distribution of solar radiation. *Solar Energy*, 10(1), 27–37. [https://doi.org/10.1016/0038-092X\(66\)90069-7](https://doi.org/10.1016/0038-092X(66)90069-7)
- [7] Kabir, E., Kumar, P., Kumar, S., Adelodun, A. A., & Kim, K.-H. (2018). Solar energy: Potential and future prospects. *Renewable and Sustainable Energy Reviews*, 82, 894–900. <https://doi.org/10.1016/j.rser.2017.09.094>
- [8] Soga, T. (2006). Chapter 1 - Fundamentals of Solar Cell. In T. Soga (Ed.), *Nanostructured Materials for Solar Energy Conversion* (pp. 3–43). Elsevier. <https://doi.org/10.1016/B978-044452844-5/50002-0>
- [9] Yusoff, Y. B. M. (2022). Subchapter 3.2 - Copper indium gallium selenide solar cells. In Akhtaruzzaman & V. Selvanathan (Eds.), *Comprehensive Guide on Organic and Inorganic*

Solar Cells (pp. 85–113). Academic Press.

<https://doi.org/10.1016/B978-0-323-85529-7.00001-3>

[10] Rashid, M. H. (2017). Power Electronics Handbook. Elsevier Science & Technology.

<http://ebookcentral.proquest.com/lib/tuee/detail.action?docID=5043418>

[11] Kim, S., Hoang, V. Q., & Bark, C. W. (2021). Silicon-Based Technologies for Flexible Photovoltaic (PV) Devices: From Basic Mechanism to Manufacturing Technologies.

Nanomaterials (Basel, Switzerland), 11(11). <https://doi.org/10.3390/nano11112944>

[12] Spalatu, N., Hiie, J., Krunks, M., & Mikli, V. (2017). Development of CdTe absorber layer for thin-film solar cells.

<https://digikogu.taltech.ee/et/Item/e75b8aee-267f-4a13-837e-bb6db6923c61>

[13] Lee, T. D., & Ebong, A. U. (2017). A review of thin film solar cell technologies and challenges. Renewable and Sustainable Energy Reviews, 70, 1286–1297.

<https://doi.org/10.1016/j.rser.2016.12.028>

[14] Acik, I. O. (n.d.). DEVELOPMENT OF Sb₂Se₃ THIN FILM SOLAR CELLS BY CLOSE-SPACED SUBLIMATION Sb₂Se₃ õhukesekileliste päikesepatareide arendamine lähidistants-sublimatsiooni meetodil.

<https://digikogu.taltech.ee/testimine/en/Download/27ec5a07-a0b6-43a4-b689-f0919680ac58/Sb2Se3hukesekilelistepikesepatareidearendamin.pdf>

[15] Mohammad Bagher, A. (2015). Types of solar cells and application. American Journal of Optics and Photonics, 3(5), 94. <https://doi.org/10.11648/j.ajop.20150305.17>

[16] Deng, X., & Schiff, E. A. (2003). Amorphous Silicon Based Solar Cells.

<https://surface.syr.edu/phy/47/>

[17] Mufti, N., Amrillah, T., Taufiq, A., Sunaryono, Aripriharta, Diantoro, M., Zulhadjri, & Nur, H. (2020). Review of CIGS-based solar cells manufacturing by structural engineering. Solar Energy, 207, 1146–1157. <https://doi.org/10.1016/j.solener.2020.07.065>

[18] Heywang, W., & Zaininger, K. H. (2004). Silicon: the Semiconductor Material. In P.

- Siffert & E. F. Krimmel (Eds.), *Silicon: Evolution and Future of a Technology* (pp. 25–42). Springer Berlin Heidelberg. https://doi.org/10.1007/978-3-662-09897-4_2
- [19] Lavaa, A. (2021, January 19). What is Monocrystalline Solar Panel? Advantages and Disadvantages. *Industrial Manufacturing Blog | Linqip*.
<https://www.linqip.com/blog/what-is-a-monocrystalline-solar-panel/>
- [20] Kondrotas, R., Chen, C., & Tang, J. (2018). Sb₂S₃ Solar Cells. *Joule*, 2(5), 857–878.
<https://doi.org/10.1016/j.joule.2018.04.003>
- [21] Kärber, E., Katerski, A., Oja Acik, I., Mere, A., Mikli, V., & Krunks, M. (2016). Sb₂S₃ grown by ultrasonic spray pyrolysis and its application in a hybrid solar cell. *Beilstein Journal of Nanotechnology*, 7, 1662–1673. <https://doi.org/10.3762/bjnano.7.158>
- [22] Zeng, Y., Sun, K., Huang, J., Nielsen, M. P., Ji, F., Sha, C., Yuan, S., Zhang, X., Yan, C., Liu, X., Deng, H., Lai, Y., Seidel, J., Ekins-Daukes, N., Liu, F., Song, H., Green, M., & Hao, X. (2020). Quasi-Vertically-Orientated Antimony Sulfide Inorganic Thin-Film Solar Cells Achieved by Vapor Transport Deposition. *ACS Applied Materials & Interfaces*, 12(20), 22825–22834. <https://doi.org/10.1021/acsami.0c02697>
- [23] Zimmermann, E., Pfadler, T., Kalb, J., Dorman, J. A., Sommer, D., Hahn, G., Weickert, J., & Schmidt-Mende, L. (2015). Toward High-Efficiency Solution-Processed Planar Heterojunction Sb₂S₃ Solar Cells. *Advancement of Science*, 2(5), 1500059.
<https://doi.org/10.1002/adv.201500059>
- [24] Eensalu, J. S., Katerski, A., Kärber, E., Weinhardt, L., Blum, M., Heske, C., Yang, W., Oja Acik, I., & Krunks, M. (2019). Semitransparent Sb₂S₃ thin film solar cells by ultrasonic spray pyrolysis for use in solar windows. *Beilstein Journal of Nanotechnology*, 10, 2396–2409. <https://doi.org/10.3762/bjnano.10.230>
- [25] Han, J., Pu, X., Zhou, H., Cao, Q., Wang, S., He, Z., Gao, B., Li, T., Zhao, J., & Li, X. (2020). Synergistic Effect through the Introduction of Inorganic Zinc Halides at the Interface

of TiO₂ and Sb₂S₃ for High-Performance Sb₂S₃ Planar Thin-Film Solar Cells. *ACS Applied Materials & Interfaces*, 12(39), 44297–44306.

<https://doi.org/10.1021/acsami.0c11550>

[26] Wang, S., Zhao, Y., Che, B., Li, C., Chen, X., Tang, R., Gong, J., Wang, X., Chen, G., Chen, T., Li, J., & Xiao, X. (2022). A Novel Multi-Sulfur Source Collaborative Chemical Bath Deposition Technology Enables 8%-Efficiency Sb₂S₃ Planar Solar Cells. *Advanced Materials*, 34(41), e2206242. <https://doi.org/10.1002/adma.202206242>

[27] Zhang, L., Jiang, C., Wu, C., Ju, H., Jiang, G., Liu, W., Zhu, C., & Chen, T. (2018). V₂O₅ as Hole Transporting Material for Efficient All Inorganic Sb₂S₃ Solar Cells. *ACS Applied Materials & Interfaces*, 10(32), 27098–27105.

<https://doi.org/10.1021/acsami.8b09843>

[28] Jin, X., Yuan, Y., Jiang, C., Ju, H., Jiang, G., Liu, W., Zhu, C., & Chen, T. (2018). Solution processed NiO_x hole-transporting material for all-inorganic planar heterojunction Sb₂S₃ solar cells. *Solar Energy Materials & Solar Cells*, 185, 542–548.

<https://doi.org/10.1016/j.solmat.2018.06.017>

[29] Ito, S., Tsujimoto, K., Nguyen, D.-C., Manabe, K., & Nishino, H. (2013). Doping effects in Sb₂S₃ absorber for full-inorganic printed solar cells with 5.7% conversion efficiency. *International Journal of Hydrogen Energy*, 38(36), 16749–16754.

<https://doi.org/10.1016/j.ijhydene.2013.02.069>

[30] Juneja, N., Mandati, S., Katerski, A., Spalatu, N., Daskeviciute-Geguziene, S., Vembris, A., Karazhanov, S., Getautis, V., Krunkis, M., & Acik, I. O. (2022). Sb₂S₃ solar cells with a cost-effective and dopant-free fluorene-based enamine as a hole transport material. *Sustainable Energy & Fuels*, 6(13), 3220–3229.

<https://doi.org/10.1039/D2SE00356B>

[31] Holliday, S., Ashraf, R. S., Wadsworth, A., Baran, D., Yousaf, S. A., Nielsen, C. B., Tan, C.-H., Dimitrov, S. D., Shang, Z., Gasparini, N., Alamoudi, M., Laquai, F., Brabec, C. J.,

- Salleo, A., Durrant, J. R., & McCulloch, I. (2016). High-efficiency and air-stable P3HT-based polymer solar cells with a new non-fullerene acceptor. *Nature Communications*, 7, 11585. <https://doi.org/10.1038/ncomms11585>
- [32] Rombach, F. M., Haque, S. A., & Macdonald, T. J. (2021). Lessons learned from spiro-OMeTAD and PTAA in perovskite solar cells. *Energy & Environmental Science*, 14(10), 5161–5190. <https://doi.org/10.1039/D1EE02095A>
- [33] PubChem. (n.d.). Spiro-OMeTAD. Retrieved March 21, 2023, from <https://pubchem.ncbi.nlm.nih.gov/compound/Spiro-OMeTAD>
- [34] de Leon, A., & Advincula, R. C. (2015). Chapter 11 - Conducting Polymers with Superhydrophobic Effects as Anticorrosion Coating. In A. Tiwari, J. Rawlins, & L. H. Hihara (Eds.), *Intelligent Coatings for Corrosion Control* (pp. 409–430). Butterworth-Heinemann. <https://doi.org/10.1016/B978-0-12-411467-8.00011-8>
- [35] Khan, A. U., Kumar, L., Islam, T., & Khan, M. E. (2021). Fabrication of Nanostructured Metal Oxide Thin Film Capacitive Humidity Sensor. In S. Rajendran, J. Qin, F. Gracia, & E. Lichtfouse (Eds.), *Metal and Metal Oxides for Energy and Electronics* (pp. 355–374). Springer International Publishing. https://doi.org/10.1007/978-3-030-53065-5_10
- [36] Sung, S.-J., Gil, E. K., Lee, S.-J., Choi, Y. C., Yang, K.-J., Kang, J.-K., Cho, K. Y., & Kim, D.-H. (2017). Systematic control of nanostructured interfaces of planar Sb₂S₃ solar cells by simple spin-coating process and its effect on photovoltaic properties. *Journal of Industrial and Engineering Chemistry*, 56, 196–202. <https://doi.org/10.1016/j.jiec.2017.07.012>
- [37] Chen, X., Hu, Y., Xie, Z., & Wang, H. (2018). Chapter 3 - Materials and Design of Photocatalytic Membranes. In A. Basile, S. Mozia, & R. Molinari (Eds.), *Current Trends and Future Developments on (Bio-) Membranes* (pp. 71–96). Elsevier. <https://doi.org/10.1016/B978-0-12-813549-5.00003-7>
- [38] Spin coating: Complete guide to theory and techniques. (n.d.). Ossila. Retrieved

January 28, 2023, from <https://www.ossila.com/en-eu/pages/spin-coating>

[39] Rehg, T. J., & Higgins, B. G. (2014). *Evaporative Convection in Spin Coating*.

University of California Davis: Davis, CA, USA.

https://www.researchgate.net/profile/Brian-Higgins/publication/261133233_Evaporative_Convection_in_Spin_Coating/links/00b4953343438275a6000000/Evaporative-Convection-in-Spin-Coating.pdf

[40] Ukoba, K. O., Eloka-Eboka, A. C., & Inambao, F. L. (2018). Review of nanostructured NiO thin film deposition using the spray pyrolysis technique. *Renewable and Sustainable Energy Reviews*, 82, 2900–2915. <https://doi.org/10.1016/j.rser.2017.10.041>

[41] Park, S.-I., Quan, Y.-J., Kim, S.-H., & Ahn, S.-H. (n.d.). Fig. 8. Scheme of spray pyrolysis technique films of any composition. ResearchGate. Retrieved April 19, 2023, from https://www.researchgate.net/figure/Scheme-of-spray-pyrolysis-technique-films-of-any-composition-This-technique-produces_fig6_309018906

[42] Bashir, A., Awan, T. I., Tehseen, A., Tahir, M. B., & Ijaz, M. (2020). Chapter 3 - Interfaces and surfaces. In T. I. Awan, A. Bashir, & A. Tehseen (Eds.), *Chemistry of Nanomaterials* (pp. 51–87). Elsevier. <https://doi.org/10.1016/B978-0-12-818908-5.00003-2>

[43] Kosasih, F. U., Erdenebileg, E., Mathews, N., Mhaisalkar, S. G., & Bruno, A. (2022). Thermal evaporation and hybrid deposition of perovskite solar cells and mini-modules. *Joule*, 6(12), 2692–2734. <https://doi.org/10.1016/j.joule.2022.11.004>

[44] Hughes, M. (2013a, September 30). What is thin film deposition by thermal Evaporation? Semicore Equipment Inc; Semicore, Inc.

<https://www.semicore.com/news/71-thin-film-deposition-thermal-evaporation>

[45] Park, S.-I., Quan, Y.-J., Kim, S.-H., Kim, H., Kim, S., Chun, D.-M., Lee, C. S., Taya, M., Chu, W.-S., & Ahn, S.-H. (2016). A review on fabrication processes for electrochromic devices. *International Journal of Precision Engineering and Manufacturing-Green Technology*, 3(4), 397–421. <https://doi.org/10.1007/s40684-016-0049-8>

- [46] Depla, D., Mahieu, S., & Greene, J. E. (2010). Chapter 5 - Sputter Deposition Processes. In P. M. Martin (Ed.), *Handbook of Deposition Technologies for Films and Coatings* (Third Edition) (pp. 253–296). William Andrew Publishing.
<https://doi.org/10.1016/B978-0-8155-2031-3.00005-3>
- [47] Hughes, M. (2013b, October 7). Thin film deposition by sputtering: Essential basics. Semicore Equipment Inc; Semicore, Inc.
<https://www.semicore.com/news/70-thin-film-deposition-sputtering>
- [48] Whittig, L. D., & Allardice, W. R. (2018). X-Ray Diffraction Techniques. In *Methods of Soil Analysis* (pp. 331–362). Soil Science Society of America, American Society of Agronomy. <https://doi.org/10.2136/sssabookser5.1.2ed.c12>
- [49] Ripoll, M. M. (n.d.). Crystallography. Scattering and diffraction. The Bragg's Law. Retrieved February 16, 2023, from
https://www.xtal.iqfr.csic.es/Cristalografia/parte_05_5-en.html
- [50] Vernon-Parry, K. D. (2000). Scanning electron microscopy: an introduction. III-Vs Review: *The Advanced Semiconductor Magazine*, 13(4), 40–44.
[https://doi.org/10.1016/S0961-1290\(00\)80006-X](https://doi.org/10.1016/S0961-1290(00)80006-X)
- [51] People, O. (2018, April 9). Scanning electron microscopy. *Nanoscience Instruments*.
<https://www.nanoscience.com/techniques/scanning-electron-microscopy/>
- [52] Picollo, M., Aceto, M., & Vitorino, T. (2019). UV-Vis spectroscopy. *Physical Sciences Reviews*, 4(4). <https://doi.org/10.1515/psr-2018-0008>
- [53] Üürike, M. (n.d.). Influence of pH on the properties of chemically deposited CdS thin films and solar cells. Tallinn University of Technology.
- [54] Pazoki, M., Cappel, U. B., Johansson, E. M. J., Hagfeldt, A., & Boschloo, G. (2017). Characterization techniques for dye-sensitized solar cells. *Energy & Environmental Science*, 10(3), 672–709. <https://doi.org/10.1039/C6EE02732F>
- [55] Solar cell characterization & testing. (n.d.). Ossila. Retrieved March 11, 2023, from

<https://www.ossila.com/en-eu/pages/solar-cell-testing>

[56] Quantum efficiency. (n.d.). Retrieved March 11, 2023, from

<https://www.pveducation.org/pvcdrom/solar-cell-operation/quantum-efficiency>

[57] Eensalu, J. S., Katerski, A., Kärber, E., Oja Acik, I., Mere, A., & Krunks, M. (2019).

Uniform Sb₂S₃ optical coatings by chemical spray method. *Beilstein Journal of Nanotechnology*, 10, 198–210.

[58] Eensalu, J. S., Katerski, A., Kärber, E., Weinhardt, L., Blum, M., Heske, C., Yang, W., Oja Acik, I., & Krunks, M. (2019). Semitransparent Sb₂S₃ thin film solar cells by ultrasonic spray pyrolysis for use in solar windows. *Beilstein Journal of Nanotechnology*, 10, 2396–2409.

[59] Koltsov, M. (2021). EFFECT OF TiO₂ ANNEALING CONDITIONS ON THE PERFORMANCE OF ANTIMONY SELENIDE THIN FILM SOLAR CELL

TiO₂ kiledelõõmutamise mõju õhukesekilelise antimonseleniidi päikesepatarei tõhususele MASTER THESIS. digikogu.taltech.ee.

<https://digikogu.taltech.ee/et/Download/23541d6b-592f-4f67-9d28-11451920236b/TiO2kiledelmutamisemjuhukesekileliseantim.pdf>